12-2023

Characterization of Interlayer Laser Shock Peening during Fused Filament Fabrication of Polylactic Acid (PLA)

Fabien Denise
University of Nebraska-Lincoln, fdenise2@huskers.unl.edu

CHARACTERIZATION OF INTERLAYER LASER SHOCK PEENING DURING FUSED FILAMENT FABRICATION OF POLYLACTIC ACID (PLA)

by

Fabien Denise

A THESIS

Presented to the Faculty of

The Graduate College at the University of Nebraska

In Partial Fulfillment of Requirements

For the Degree of Master of Science

Major: Mechanical Engineering and Applied Mechanics

Under the Supervision of Professor Michael P. Sealy

Lincoln, Nebraska

December 2023

CHARACTERIZATION OF INTERLAYER LASER SHOCK PEENING DURING FUSED FILAMENT FABRICATION OF POLYLACTIC ACID (PLA)

Fabien Denise, M.S.

University of Nebraska, 2023

Advisor: Michael P. Sealy

The field of additive manufacturing (AM) has gained a significant amount of popularity due to the increasing need for more sustainable manufacturing techniques and the adaptive development of complex product geometries. The problem is that AM parts routinely exhibit flaws or weaknesses that affect functionality or performance. Over the years, surface treatments have been developed to compensate certain flaws or weaknesses in manufactured products. Combining surface treatments with the modularity of additive manufacturing could lead to more adaptable and creative improvements of product functions in the future. The current work evaluates the feasibility of pursuing a new research axis in the field of additive manufacturing for mechanical and chemical treatments during the making of polymers. The interest here is to investigate the effects of combining laser shock peening (LSP) in a multilayer AM product by introducing interlayer surface treatments that cold work the temporarily exposed layer. Shot peening has already proven effective at increasing mechanical strength of polymer materials in interlayer peening processes by locally inducing compressive residual stresses (CRSs). However, only few publications concern LSP on polymers, this could be due to the high-energy output of lasers that seems incompatible with the low tensile strength of polymers. In addition to evaluating this assumption, this project has the goal of exploring the effects of peening on different layers. Traditionally,

each peened layer is separated by a fix number of unpeened layers, commonly referred to as fixed interval hybrid AM. However, ideal solutions for peening layer intervals are hypothesized to be irregular. Here, the aim was to study more diverse distribution patterns by comparing periodic and irregular intervals. Since the understanding of the effects of LSP on polymers is very limited, different aspects of thermo-mechanical behavior were evaluated.

ACKNOWLEDGEMENTS

My special thanks go to my advisors and committee members Dr. Michael P. Sealy, Dr. Laurent Delbreilh, Dr. Mehrdad Negahban, and Dr. Allison Saiter-Fourcin for their guidance and helping me grow professionally both as a student and as a scientist. I also need to thank Dr. Benoit Vieille for providing his expertise, laboratory, and equipment at INSA Rouen for crack monitoring of hybrid samples. I would like to thank both the University of Rouen, Normandy and the University of Nebraska, Lincoln for the opportunity to receive a dual degree. I thank the directors of the MEME program, Dr. Li Tan and Dr. Nicolas Delpouve, for their support needed to pursue this research project. I would also like to thank the laboratory technicians of both at the N.E.A.T. Lab and at the G.P.M.: Mark Stroup, Andrew Menendez, Marie-Rose Garda, and Eric Dontzoff. Their assistance on the various experiments was extremely valuable. Lastly, I need to address my special thanks to George Klein, Haitham Hadidi, and Victor Tanguy for their contribution on this project.

This work was supported in part by NSF CMMI: 1846478. The University of Rouen, Normandy and the international credit mobility ERASMUS+ funded research activity and travel to the United States. Lastly, I would like to acknowledge financial support in part from the French Agence Nationale de la Recherche LabEx EMC3 through Project HAMMO (Grant No. 10-LABX-0009).

DEDICATION

I dedicate this thesis to my friends Swann, Antoine, and Sabrina who provided essential moral support during difficult times.

CONTENTS

LIST OF TABLES

LIST OF FIGURES

LIST OF ABBREVIATIONS AND SYMBOLS

AM	Additive manufacturing
3D	3 dimensional
FDM	Fused deposition modeling
FFF	Fused filament fabrication
CRS	Compressive residual stress
SLA	stereolithography
PBF	Powder bed fusion
UV	Ultraviolet
DIW	Direct ink writing
GelMA	Gelatin methacrylate
LSP	Laser shock peening
SP	Shot peening
DSC	Differential scanning calorimetry
DMA	Dynamic mechanical analysis
PLA	Polylactic acid
Nd:YAG	Neodymium-doped yttrium aluminum garnet
NEAT	Nebraska engineering additive technology
GPM	Groupe de Physique des Matériaux
Tg	Glass transition temperature
Tm	Melting temperature
℃	Temperature in Celsius
GPa	Gigapascal
W	Watt

V	Volt
J	Joule
Hz	Hertz
A	Acceleration
P	Load
N	Newton
kN	Kilo Newton
k_B	Stiffness
κ_{max}	Curvature
d	Distance
δ_{mid}	Middle point displacement
U	Strain energy density
M	Moment
m	Meter
mm	millimeter
ms	millisecond
h	Height
E’	Storage modulus
E”	Loss modulus
E	Edge orientation
F	Flat orientation

ORGANIZATION OF THESIS

This document compiles the motivations, challenges, experiments, and insights relative to the characterization of the effects of interlayer laser peening a multilayer polymer material on its thermos-mechanical properties. Chapter 1 provides an overview of: hybrid AM, LSP, other surface treatment methods and how polymer materials interact with these different subjects. The current challenges of these industries and how hybrid AM is well positioned to solve them will also be discussed. Chapter 2 provides a detailed description of fabrication for the samples used during the experiments, notably how LSP is applied in the context of a hybrid AM process. The various challenges related to the fabrication process itself will be highlighted. Chapter 3 describes the low velocity impact experiment with its specific objectives, set-up, and results. A summary of the knowledge gained during this experiment is also provided in this chapter. Chapter 4 describes the impact of LSP on the viscoelastic behavior of the studied material through a dynamic mechanical analysis. A summary of the knowledge gained during this experiment is also provided in this chapter. Chapter 5 relates the three-point bending experiment conducted in complement of the low velocity impact test. The objective was to visualize the deformation. Finally, Chapter 6 compiles the results and analysis from the previous chapter to offer suggestions on focus points for future studies.

CHAPTER 1

STATE-OF-THE-ART IN LASER SHOCK PEENING DURING ADDITIVE MANUFACTURING OF POLYMERS

1.1 The need for AM in the industry

Additive manufacturing (AM) is a set of manufacturing processes that are capable of producing parts directly from a computer model of the part [1], unlike conventional manufacturing techniques AM doesn't involve excessive removal and shaping of material by mechanical procedures to achieve the final product [2]. With the progress of industrial processes and the increasing need for complex parts, AM processes have become very prevalent in various industrial sectors, including aerospace, automotive, medical, architecture, arts and design, food, and construction [3]. The main appeal of AM is making single complex parts or construction easier and faster compared to traditional manufacturing, especially with hard to shape materials like concrete [1] or metals [4]. This leads to higher precision for very specific geometries.

Another important aspect of AM is the ability to repurpose. It is often mentioned how energy and material efficiency need to work together in order to achieve sustainable AM processes [5]. With Earth's resources depleting, it is detrimental to achieve more sustainable manufacturing quickly for which AM has a big role to play in the matter. Some industries like automotive, aerospace and medical have been using AM processes for years but mainly for prototyping. What is observed now is a shift toward using these technologies in larger scale production. Technologies like 3D printing allow not only for less waste in input materials but also incentivizes reuse

because scraps in most 3D printing techniques can be remanufactured into raw input materials [6]. Some industries are already using recycled materials as source for 3D printing [7]. AM can also help reduce the supply chain complexity. With one printer capable of producing complex geometries, there is no need for multiple manufacturing tools and machines to create a single part.

Between 2020 and 2021, 88 research studies were published regarding the use of AM for sustainability purposes [8], and the number is still increasing. In 2023, the European Commission published a draft for new regulations to come regarding eco-designing products, recyclability, and sustainability of products. With governments pushing industries to put more sustainable goods on the market, it is obvious that AM will gain an exponential amount of interest and will be implemented to an even greater extend in all manufacturing industries in the years to come. However, a lot of AM reviews tend to focus on the material science aspect of these processes [9]. This fixation is understandable. With certain industries being very demanding about material performances, AM helps to solve the problem of getting the most out of the raw material that is given.

AM does not provide a guarantee of quality or the removal of all defects in a part. Therefore, combining the benefits of both traditional manufacturing and additive manufacturing methods could offer a new design paradigm to improve functional performance. A big emphasis is put on researching the potential benefits of this so called “hybrid additive manufacturing” [2].

There are many ways to combine traditional and AM processes, whether it involves pre-heating a part with a laser to assist cutting and shaping [2] or machining 3D printed parts. All the possible combinations have specific purposes that can help make manufacturing easier or more effective and sometimes improve the characteristics

of the built part. In this perspective, a lot of research has focused on increasing a 3D printed part's physical properties, whether it is mechanical strength, fatigue, or anticorrosion properties by applying post treatments like mechanical or chemical surface treatments [10,11]. Although these post treatments are common in manufacturing, combining them with the layer-by-layer method of building can offer new perspectives for improving a raw material's defects. With the wide range of AM processes and various existing post treatments, hybrid AM opens new possibilities that could be explored in the future.

1.2 3D printing technologies

One type of manufacturing method that has exponentially grown in popularity in the recent years is 3D printing [12,13]. A lot of progress has been made on what materials can be 3D printed in polymers, ceramics, metals, and composites. The choice of 3D printing method will depend on the purpose, material properties, and manufacturability (*i.e.*, pintability [14], melting point, or sensitivity to ultraviolet light). Extrusion based 3D printing uses a nozzle to deposit a semi-solid material, usually in flowing form that will solidify over time or after post treatment [3]. The most commonly used technologies in the industry are: fused deposition modeling (FDM), which uses a heated polymer filament that is extruded through the nozzle with pressure [15] and contour crafting, which has the particularity to utilize a scrapping tool to smoothen the exterior profile to enhance the surface finish of the extruded object [16]. Fused filament fabrication (FFF) is an extrusion-based building method very similar to FDM meaning they both use a polymer filament fed through the nozzle. The main differences between FFF and FDM are [17,18]: (a) the price, FFF is much more affordable that FDM; (b) the quality of printed objects, being cheaper also means that

FFF gives you a lot less control over the print and rougher surfaces due to less printing precision; (c) mechanical properties of printed objects, the heat cycles are a lot more precise in FDM resulting in better reduced residual stress in the final piece; and (d) the accessibility, FFF machines are usually designed for easy set-up and easy to run where FDM are a lot more professional. The choice between these two technologies will depend on the use made and the requirements in every aspect of the project. FFF being a more "casual" technology does not mean it is not suited for research purposes [17,19] if the goal is to alter the final product to study the effects on a material's properties or if surface quality is not primordial. FDM can be excessive. Methods may vary depending on the material used. For instance, powder bed fusion is mostly used for metals [3] while technologies like binder jetting or material extrusion are mostly used for polymer type material. Despite its many advantages, 3D printing still faces important challenges. For instance, the limited number of material that combine good printability and biocompatibility while reducing the fabrication costs is not pushing the pharmaceutical industry to heavily invest in this technology [14,17]. While the potential of this technology is fascinating, concerted collaborative and well supervised studies are necessary in order to optimize all the related process in order to guarantee products quality at an industrial level [20].

1.3 Surface treatments in additive manufacturing

Peening is a post treatment method involving mechanically shocking a material to improve its physical properties. The peening process in AM takes three main forms: shot peening (SP), ultrasonic peening, and laser shock peening (LSP). SP remains the most widely used process to introduce compressive residual stress (CRS) [21,22] in

different materials due to the low equipment cost. In the past twenty years, the scientific community has grown a great interest for LSP.

Studies have shown that in the case of metals, LSP produces compressive residual stresses to a deeper level as well as significantly improving fatigue performances [23]. LSP has also proven to harden the surface and improve the mechanical properties of some structural metal components such as carbon steels, stainless steels, cast irons, aluminum alloys, titanium alloys, and nickel based super-alloys [21,24]. A number of studies have investigated the in-depth effects of LSP on metals, such as tailoring and controlling the residual stress profile of parts, made by selective laser melting [25]. This study is more interested in the combination of LSP with powder bed fusion process as it is comparable to the one used for our polymer samples.

It has been shown that the extensive application of LSP between printed layers increased the ability of 420 stainless steel to endure higher deformation and attain a higher toughness [26]. It has been shown that combining SP with FFF printing, the mechanical and thermal properties of polymer materials can indeed be altered [27,28]. Furthermore, preliminary results suggest the layer pattern on which you apply the peening (meaning how many layers are peened in the total amount of layers) has a drastic impact on the polymer's properties. For instance, only peening the surface of the samples seem to be the least effective method giving no significant benefit over the non-peened samples. On the other hand, hybrid peening patterns have been found to improve the samples energy abortion potential. This result must take into consideration that only a small range of patterns have been tested, and their efficiency is highly dependent on the printing orientation. A side strip (45°/-45°) printing orientation was proven to be the most effective when combined with any peening pattern [28]. Even

though a most efficient peening pattern was indeed found in the studies that took interest in the matter, a possibility for even better performances by changing the pattern could be investigated.

1.4 Polymers in additive manufacturing

In 2021, the global polymer market was valued at $590 billion in 2021 and is expected to exceed $900 billion by 2030 [29]. With the development of composite materials, partially countering the relatively weak mechanical properties of polymers, and their great flexibility when it comes to manufacturing, polymers are now a big part of raw materials used in almost every industry. One of the contributing factors for their exponential growth in the last years is the natural compatibility between certain polymers and AM processes. The different existing AM technologies are adapted for various types of polymers that can typically be classified into four categories: photosensitive resins, thermoplastic powders, thermoplastic filaments and viscous polymer inks [30]. Photosensitive resins are used in combination with vat photopolymerization, a liquid prepolymer is locally hardened from cross-linking using an appropriate laser. Photosensitive resins can be classified based on their type (photoinitiators, monomers, oligomers and additives) or their usage (biocompatible, shape memory, digital multi-materials) [15] and they can be used to make composite resins that combine the functionality of resin and the fibers [4]. The layer height can be adjusted on modern printers (*e.g.*, Formlabs SLA (stereolithography) 3D printers) to adjust between print speed and quality [20,30]. Advanced compact SLA 3D printer and development of innovative SLA resin formulations with a wide range of optical, mechanical and thermal properties matching those of commodity. engineering and industrial thermoplastics accelerates innovation and provide opportunities to support

companies across a wide range of industries including manufacturing, dentistry, healthcare, education, entertainment, jewelry, audiology, *etc.* [3]. Thermoplastics can come into powder or filament form, the main difference being the technologies used to exploit these medium. Thermoplastics can be classified into two categories based on their microstructure:

(1) Amorphous thermoplastics' (*e.g.*, polystyrene, polycarbonate) molecular structures are randomly ordered giving them a degree of flexibility in solid form. Above their glass transition temperature T_g, they soften and transition to a glassy state. They do not have a defined melting point T_m.

(2) Semi-crystalline thermoplastics (*e.g.*, polyamides) have both T_m and T_g that correspond to the crystalline and amorphous regions, respectively. Above T_m, semi-crystalline thermoplastics go from solid to liquid phase with a rapid increase of viscosity [31].

Thermoplastic powders can be processed through PBF technique. This allows for high resolution prints [15] and integration of polymer blends or implementation of micro and nano-fillers during the printing process [4]. The flexibility regarding materials comes at the cost of a complex and dangerous set-up due to the usage of high-power lasers. Even though polymer composites in filament form exist, they need to be manufactured separately, and multi-material printing is not a viable option when it comes to extrusion-based technologies [30]. Viscous polymer inks are usually processed through a combination of extrusion and curing. Whether it is UV or chemical cross-linking, these techniques are regrouped under direct ink writing (DIW). Viscous polymer inks can be classified into two categories. First, highly viscous photocurable resins typically need to be irradiated via UV light after shaping to cross-link the

structure in order to retain the shape (*e.g.*, gelatin methacrylate (GelMA))[32]. Second, polymer solution inks are made by dissolving polymers into a solvent [15].

A variety of polymer solution inks are available for DIW. This includes hydrogel-based inks such as alginate and collagen that solidify by ionic and pH-controlled physical gelation, respectively [30]. However, a problem with many DIW-printed hydrogel structures is their low mechanical strength. Another approach to reliably manufacturing free-standing structures is to put the ink in a carrier bath. Gel-in-gel printing is a typical bioprinting process that uses a gel as a carrier material and is also useful when the printed structures are too weak [33]. On another note, the viscous aspect of polymer inks makes them particularly attractive for biocompatibility studies [14].

1.5 Thermo-mechanical properties characterization for polymers

Since polymeric materials can be established as one of the main sources of interest regarding AM, it is important to understand how to characterize the properties and assess the quality of both the final product and the raw material. Polymers regroup a large amount of materials with very different properties depending on their type (thermoplastics, thermosets and rubbers) and their microstructure (semi-crystalline or amorphous). Many techniques can be used to characterize these materials depending on the targeted property. In a rigid form, polymer-based materials can withstand most mechanical resistance tests such as impact or elongation. Charpy tests are very common when it comes to characterization of directed impact resistance. This type of test is especially useful when it comes to fiber reinforced composites [19], studies have used Charpy to investigate the influence of fiber orientation, size, and density on impact resistance [34]. Moreover, this notion of direction was also investigated when it comes

to filament deposition type AM processes [27], studies have used Charpy to show that orientation of the print path can influence the mechanical resistance of the final object depending on the direction of the force. Regular drop impact test can also be used to study the compression resistance of 3D printed objects [27]. However, one of the most common mechanical test for polymer based materials is the tensile test via elongation. This method is particularly useful for determining the elastic properties and limits of a material [31,35], additionally studies also use it in combination with temperature variations to investigate the thermo-mechanical properties of their material [19,28]. In parallel, methods involving both thermal and mechanical solicitations are often used to investigate the viscoelastic behavior of polymers, *e.g.*, differential scanning calorimetry (DSC) and dynamic mechanical analysis (DMA). DMA is used to investigate viscoelastic properties of polymeric materials like relaxation of the material DSC is also commonly used for studying phenomenon like crystallization and melting during thermal treatment of polymers. These parameters are particularly useful to determine the nature of the studied polymer. To go further, it is also possible to determine the composition or presence crystalline structures in polymeric materials through X-ray diffraction [31,37]. This can help with investigating the state of degradation of polymers since ultraviolet or oxygen degradation often generate new chemical groups not present in the base material [38,39].

These include some of the popular characterization methods, but other specific tools can be applied for polymers including optical, chemical, mechanical analysis or even neutron scattering [41]. Many authors have looked into the characterization techniques for polymers and have cited numerous other methods depending on the investigated parameter, with the rising popularity of polymer based composites, a

combination of multiple characterization techniques is necessary to analyze polymeric materials [42].

1.6 Aim of this study

Despite the numerous studies on polmers, the option of using laser shock peening (LSP) on polymer materials is not widely studied. Some research has shown that LSP is a suitable post-treatment process to increase the mechanical properties of some polymer-based composites [8]. However, the treatment was only applied on a surface level and used a composite material. Thus, it is impossible to determine if similar results can be obtained on a raw polymer material. The goal now is to find out to what extend one can improve the properties of polymer materials by using LSP in a multi-layer geometry. The multi-layer geometry will enable an accurate tracking of treatment zones within the fabricated part and allow characterization of properties based on treatment distribution. The possibility for better patterns will also be investigated as most studies only use regularly spaced treated layers [27]. This works aims at proving that carefully choosing where to place the treatment has an importance to move towards smarter manufacturing methods.

CHAPTER 2

SAMPLE FABRICATION

2.1 Introduction

This chapter is dedicated to the fabrication process of the samples used in this study. The samples are manufactured by a hybrid AM process that involves interlayer laser peening on 3D printed PLA plates. Each sample is supposed to illustrate the influence of peening distribution throughout the material, a specific disposition of laser treated layers and non-treated layers is called a “pattern.” The initial samples were designed with the low velocity impact test in mind (described in the Chapter 3 of this document) but as the study went on it was decided that samples used for all the experiences would originate from this original batch. The geometry was inspired by the ASTM standard D7136/D7136M [1] (Appendix 1) since it allowed for a bending resistance test when impacted as well as providing a large enough sample so it can be exploited in the future. The sample being relatively thin (4 mm in thickness) allowed for fewer possibilities in terms of peening patterns and helped to focus on more impactful patterns. The choice of patterns will be discussed first before moving on to fabrication processes.

2.2 Hybrid AM patterns

A total of seven peening patterns were chosen to highlight the wanted parameters, namely the influence of peened layers spread, the importance of stacked

layers position, and the influence of peened layers number. See the patterns below that were selected after deliberation (Figure. 2.1).

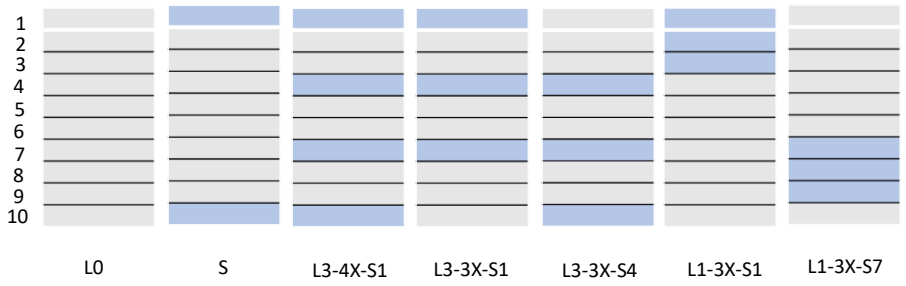

Figure 2.1 Selected laser peening patterns (peened layers are blue).

The denomination of samples works as follows:

- L(x): repartition of layers (L3 one of every three layers is peened, L1 no separation between peened layers)
- (y)X: amount of peened layers
- S(z): designation of first peened layer (see numbering on the left)

The reference pattern is unpeened L0. Another important parameter was the concentration of the peened layers in the “Top” (at n°1 layer) or “Bottom” (at n°10 layer) part of the sample. Since the plate will be bending during the impact test, most of the stresses are concentrated at its bottom, a concentration of peened layers at the top or the bottom of the sample might help to balance this phenomenon. That is why some of the patterns were similar but moved either to the top or bottom part of the sample. Finally, non-regular patterns were chosen for concentrating the peened layers in a single area. Each treated layer is partially covered by 400 dots spaced by 4.5 mm and concentrated in a square of 90 mm x 90 mm (see 2.3 Materials and Methods). This was done to reduce the peening time and laser usage since high amount of LSP had a

tendency to break some parts of the laser. The idea is that only the impacted area needs to be treated.

2.3 Materials and methods

This section describes the equipment used to 3D print and laser peen the samples as part of the hybrid AM method. All the work cited in this section was done in the NEAT labs at the UNL.

2.3.1 Fused filament fabrication

The 3D printer was a standard FFF printer from Lulzbot®. This brand was chosen since their products were accessible and some of their machines are already in use in the partner GPM lab. Thus, it was easier to find help in case of troubleshooting and conduct round robin testing. The filament used was a nano-reinforced PLA based blend manufactured by Polymaker®. The printer extruded a PLA based filament at 210 °C to form a 100 mm x 150 mm x 4 mm plate divided in 10 layers of 0.4 mm thickness. An important modification to this printer was the change of the original glass print bed to a magnetic print bed (Figure 2.2). The magnetic bed allowed removal of the sample mid-printing to peen it and then put it back on the printer to continue printing.

A calibration phase was required since the factory parameters were not always accurate to use. The main parameter to monitor was the extrusion amount. A recalibration was necessary to insure consistency between the prints. However, the precision of the print was still insufficient. When combined with the hybrid AM process, this resulted in small variations of sample thickness shown in Table 2.1.

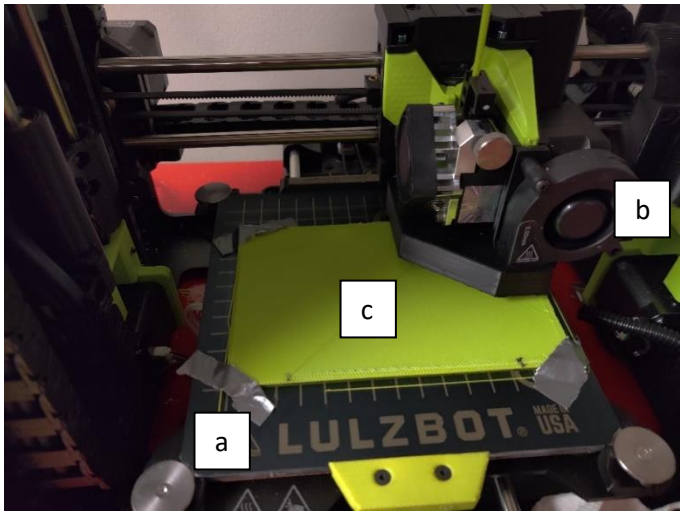

Figure 2.2 Build chamber of the Lulzbot 3D Printer: (a) magnetic print bed, (b) print head, and (c) sample being printed.

Table 2.1 Average sample thickness

Sample name	Average thickness [mm]
L0-1	4.05 ± 0.05
L0-2	4.07 ± 0.05
L0-3	4.06 ± 0.05
SP-1	4.23 ± 0.07
SP-2	4.22 ± 0.09
SP-3	4.26 ± 0.07
L34XS1-1	4.10 ± 0.07
L34XS1-2	4.09 ± 0.06
L34XS1-3	4.13 ± 0.05
L33XS1-1	4.22 ± 0.09
L33XS1-2	4.24 ± 0.05
L33XS1-3	4.24 ± 0.05
L33XS4-1	4.25 ± 0.05
L33XS4-2	4.17 ± 0.05
L33XS4-3	4.14 ± 0.05
L13XS1-1	3.96 ± 0.05
L13XS1-2	3.96 ± 0.05
L13XS1-3	3.97 ± 0.05
L13XS7-1	4.07 ± 0.05
L13XS7-2	4.03 ± 0.07
L13XS7-3	4.04 ± 0.05

Thickness of samples is obtained by averaging ten measurements randomly spread over the part geometry. Other tweaking in parameters were mainly done through the printer's software. Those parameters were modified to ensure that samples were infilled at 100% with more uniform matter distribution throughout the layers. The AM process required constantly pausing and resuming the printing process which induced a number of technical difficulties that needed solving:

- Pausing and resuming without waiting for the current layer to be finished caused the printer to be confused and reset the printhead's position. The printer would then proceed to try printing in the middle of the sample (Appendix 2). This problem could not be solved, and it usually meant that the sample was inadequate for testing.
- The print bed was heated at 60°C to ensure the adhesion of the printed object. But, constantly removing and putting the bed back on induced a rapid change in temperature at the bottom of the sample resulting in its detachment from the print bed. It was found that using weights to push down on a detached sample would sometimes stick back on the bed (Appendix 3). However, this process was uncertain and a slight change from the original position of the sample could result in the head pushing the sample out of the way and printing in midair (Appendix 4).
- The detachment of the samples sometimes was only present on the edge of the plates resulting in a slight bending of the samples (Appendix 6). Sometimes, it could be corrected by flattening the sample with weights to press down on the bended parts. This mainly resulted in uneven samples, but the middle part was good enough for me to impact.

- The constant going in and out of the printer coupled with immersion in water may also be the cause of differences in sample thickness despite having the same printing set-up.

2.3.2 Laser shock peening (LSP)

In LSP, the "impact" is induced by a plasma pocket created by a short burst of laser energy. A confinement layer was used to prevent a massive loss of energy and insure the maximum amount of CRS on the treated area. The commonly used strategy in the industry is water [2] confinement although some alternatives are being investigated with polymer-based confinement [3]. The shockwave creates localized regions of plastic deformation within the material (Figure 2.3). The pattern described by Figure 2.1 was used to peen the samples used in this study (Appendix 2).

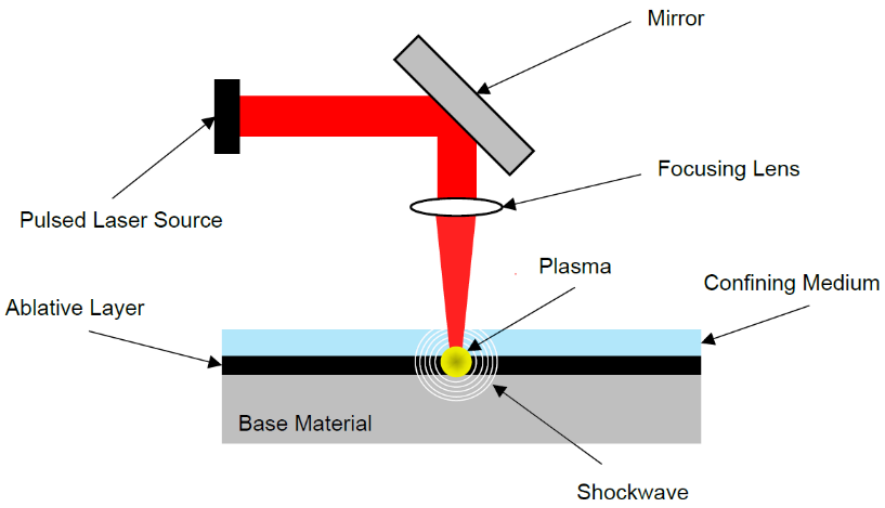

Figure 2.3 Schematic of laser shock peening (LSP) [4].

Despite the generation of high temperature plasma, LSP is a mechanical process just like SP. After focusing, the laser beam impacts an area of 2 mm diameter leaving a "dot" of same dimensions. For technical reasons, it was decided to use a partial area covering with no overlap (Figure 2.4) when studies suggest that full coverage and some overlap (meaning each dot covers a part of the previous one) provides better results in metals [4]. However, this amount of treatment is expected to be enough to observe variations in the sample's characteristics especially considering PLA is a "softer" material. It was estimated that only peening the center surface would be enough since it corresponds to the impacted area during the drop test.

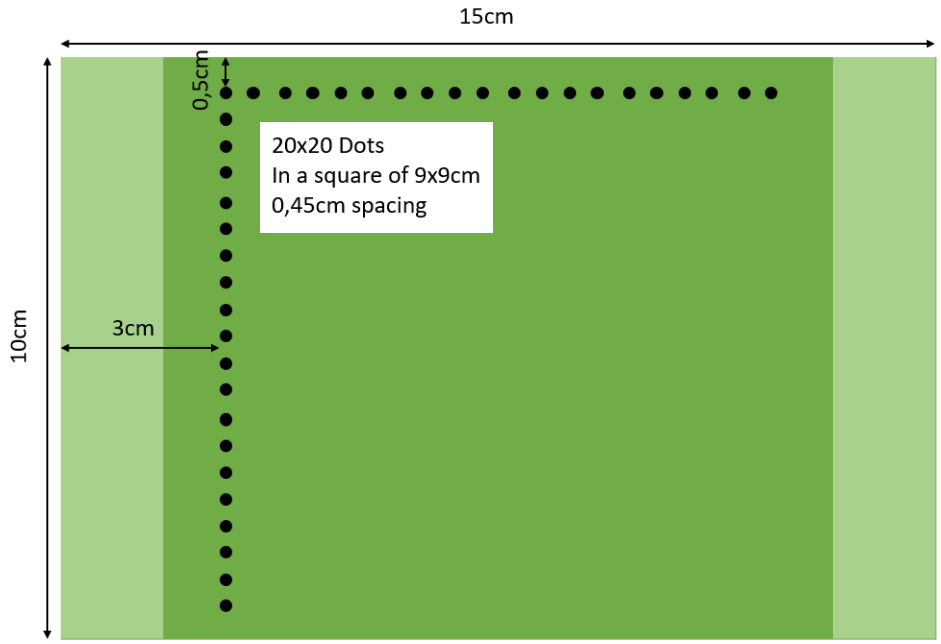

Figure 2.4 Peening area and coverage.

Peening a material using such a high-power laser requires a bit of preparation. Water confinement implies having a thin layer of water between the laser and your target with contact between the water and peened surface. There are many ways to achieve this; but, with the material at my disposition and the laser's set-up the easiest

was to submerge the sample by placing it in a container. The amount of water is of certain importance. Too much water increases the risk of deflection of the laser beam resulting in uneven spots. Too little water would not offer enough compression. Previous work showed that a roughly 3.5 mm (a tolerance margin of 0.5 mm was acceptable) thick water layer gave the best results on steel samples in a similar configuration [4].

An ablative layer was also required since small amount of plasma is still generated underwater. The layer prevents any burning and surface melting of our sample. Again, previous work showed that black electric tape provided sufficient protection but needed replacement after each peening session. The laser beam is striking the sample at an angle of 45°. The reason was to prevent water backsplash on the focusing lens. The final configuration is represented in Figure 2.5.

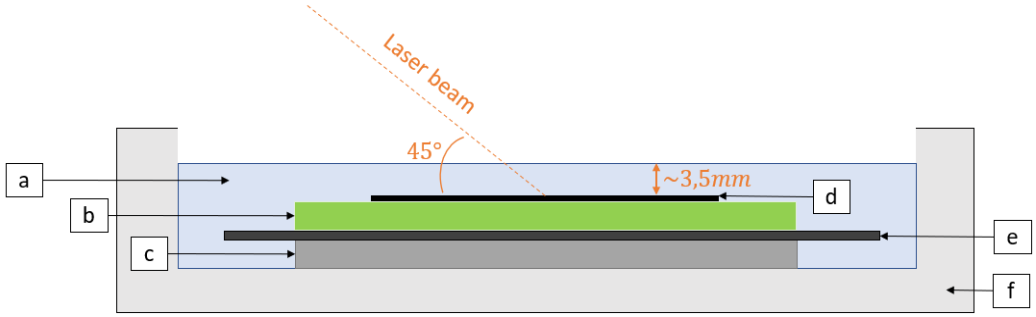

Figure 2.5 Side view of laser shock peening configuration: (a) water confinement, (b) sample, (c) support, (d) ablative tape, (e) print bed, and (f) glass container.

The pulsed laser used in these experiments was a Continuum Powerlite DLS Plus Nd:YAG laser (Appendix 7). The manufacturer's specifications are listed in Table 2.2. This laser operates within the infrared spectrum at a wavelength of 1064 nm. A high voltage oscillator and two in-series amplifiers were used to reach the maximum energy output.

Table 2.2 Continuum Powerlite DLS specifications

Energy (J)	Pulse Width (ns)	Repetition Rate (Hz)	Beam Diameter (mm)
3.0	6-9	1-10	12

The energy output can be adjusted by varying the voltage of the oscillator and/or amplifiers, the timing of the oscillator and/or amplifiers, and/or the timing of the q-switch. All the above is done through the operating software. The repetition rate can be adjusted using the q-division tool as well.

The laser was operated at the same settings for every experiment performed during this research and are as follows. These settings are presented in Table 2.3. They resulted in a laser energy output of 1.27 J. Pulse energy was defined as a 34 average output over 50 pulses measured using Ophir's PE80BF-DIF-C pyroelectric energy sensor. The q-division was set to 10 to reduce the firing rate of the laser from 10 Hz to 1 Hz. This was done to increase the control and accuracy of LSP treatments. At a firing rate of 10 Hz, the target specimen would need to move at a very high rate to avoid the destruction of the ablative layer and the accumulation of thermal effects. The water based confining layer also needed enough time to fully re-confine the surface after plasma generation.

Table 2.3 Contiuum Powerlite DLS Plus Laser Settings

Laser Setting	Potential Difference (V)	Delay (μs)
Oscillator	1400	110
Amplifier 1	1640	150
Amplifier 2	1640	150
Q Switch	-	150

The laser beam deviated from its original source by a set of mirrors and went inside the closed peening chamber through an arm (Figure 2.6). This allows for the use of a moving platform inside the chamber to automatize the peening process. The laser arm was fixed, and the beam shot out in bursts at a frequency of 1 Hz. The platform then moved according to a program that dictates its position and speed so the laser beam would strike the sample on the positions showed in Figure 2.4. The platform can move in the x, y and z axis. The height and start positions needed to be calibrated before every peening session to ensure that the spot size and peening area were as expected.

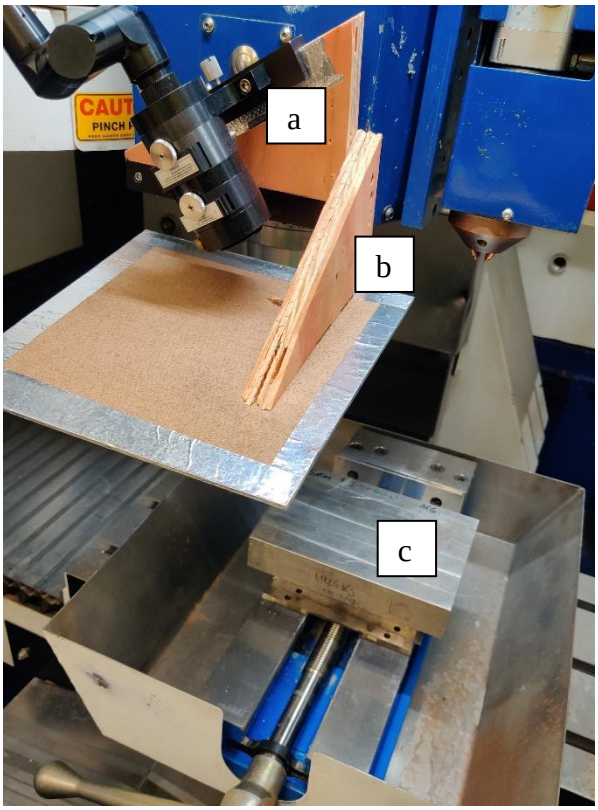

Figure 2.6 Laser configuration: (a) laser head, (b) protective screen, and (c) moving platform.

2.3.3 Limitations

The laser set-up had a couple defects that had to be worked around. The plasma ball generated during the contact between the laser beam and the sample would shoot up a beam of water. The laser head being close enough to the surface allowed water to splash on the protective lens. If that happened, the beam scattered resulting in uneven peen spots and very dangerous situations since part of the beam may go towards the inside of the chamber or outside of the peening chamber. To limit this phenomenon, the laser was placed on the side shooting towards the sample at an angle of 45°. At this angle, the energy loss was negligible. A protective screen was also installed to catch most of the water droplets going towards the laser head (Figure 2.6). Despite this configuration, small water drops still manage to get on the lens so if uneven spots are noticed the process needs to be paused and the lens cleaned.

The laser had a major issue of hyper focusing inside the deviation arm. The arm is an articulated set of mirrors and tubes that deviate the laser beam in a controlled direction. However, the mirrors inside the arm would often burn (Figure 2.7) probably due to the laser hyper focusing on specific spots resulting in unwanted high energy concentration. The mirrors burning would result in part of the beam not being reflected and energy loss at the exit point. The greater the damage, the less energy output at the end. It has been shown that an energy output of over 1.1 J was still acceptable so light damage was not a huge problem. However, the damage was very unpredictable and could happen randomly. So the energy output needed to be checked constantly. If energy went under 1.1 J, the damaged mirror needed to be replaced. Mirrors for this laser are very expensive and changing them was a time-consuming process. This was a huge problem, but the source of damage was uncertain since this installation was very new and no one dug into this issue yet.

Figure 2.**7** Slight but noticeable mirror damage.

2.4 Summary and Conclusions

A hybrid AM process combining FFF 3D printing and LSP was used to manufacture PLA-based multi-layered plates. Strategic locations were chosen for the application of LSP throughout the samples to test out the following hypothesis: (a) non-regular distribution of LSP could be beneficial and (b) there is a potential to optimize the distribution and number of treated layers. In total, three replicate samples were fabricated for each of the seven selected peening patterns making 21 samples in total. Some of the difficulties came from the lack of experience with the process, resulting in sub-optimal manufacturing time and sample quality. In the future, the combination of 3D printing and LSP needs to be done through a more ergonomic process and the reliability of the laser used needs to be optimized.

CHAPTER 3

LOW VELOCITY IMPACT

3.1 Introduction

Initially, an impact test was chosen because it was used in previous work concerning SP on polymer and metal samples done in the NEAT Lab. This provides a good reference point for the future results. However, a new sample geometry was chosen changing the impact test from a compressive behavior study to a bending resistance study similar to a three-point bending set-up. The sample was 4 mm in thickness, which allows for a repartition in 10 layers versus the 40 mm thick sample divided in over 100 layers used for compressive impact tests [1].

3.2 Materials and methods

The drop test set-up allowed the plate to be impacted in the center and bend as it was absorbing the impact. A schematic of which is given in Figure 3.1. An impact head was released from a selected height and allowed to free fall until hitting the sample. A guide rail assured a straight trajectory. The support was high enough so that if the plates bent too much and cracked, the impact head would not hit the anvil.

The drop tower was manufactured by Cadex Inc. The drop test was initiated by a software given by Cadex that also recorded the results from the accelerometer placed in the impactor. Measured values were the acceleration value A (in G's) as well as the load on impact P (in kN) given by a load cell placed under the anvil. The key components of the tower are listed below (refer to Figure 3.2 for visuals)

- Rail: guides the drop head on its way up and down
- Drop head assembly: weighs 4,317 kg with the impactor; is the part that will come in contact with the test subject
- Accelerometer: records the acceleration of the head in G's (inside the impactor)
- Anvil: supports the test subject
- Time gate: records the time at which the drop head impacts the test subject
- Flyer: acts as a trigger for the time gate
- Stopper: prevents head from hitting the anvil too hard and damaging each other
- Control panel: allows the user to manually move the head up and down

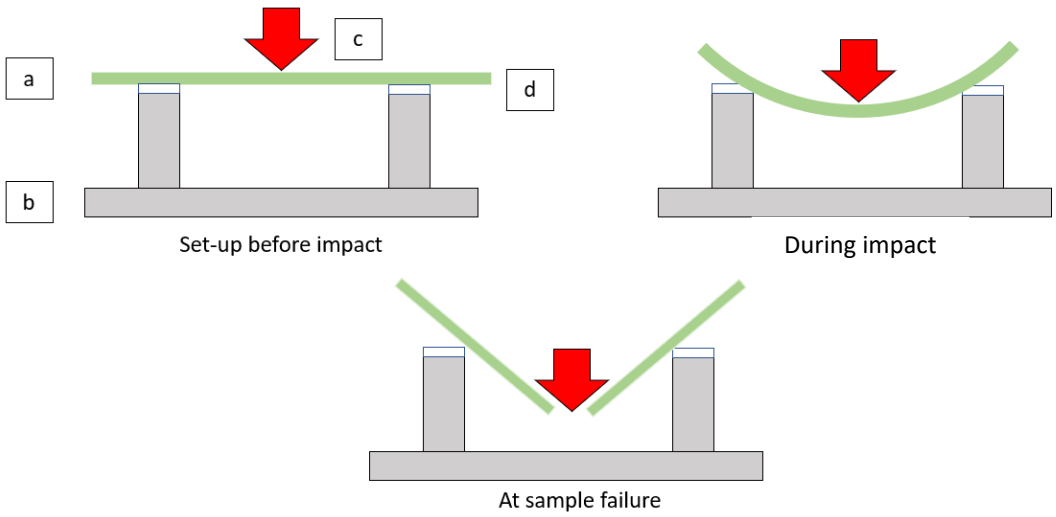

Figure 3.1 Impact schematics: (a) sample, (b) steal support, (c) impactor, and (d) double sided tape.

Setting up and operating the drop tower was straight forward as previous NEAT Lab members have already worked with this machine. The main parameters that needed to be monitored were as follows:

- The drop head needed to be in contact with the sample before initiating the drop.

- The stopper needed to be lower than the sample but higher than the anvil so that it will stop the head but not so soon that it influenced the recorded acceleration on impact.
- The time gate needed to be set up right above the flyer of the drop head assembly (Figure 3.2 [e,f]) before initiating the drop.

Starting at 10 cm drop height, if an impact was not enough to break the sample, the height would be increased by a small amount working by increments of 10 cm ranging from 10 to 40 cm and then increments of 5 cm until failure. This method was chosen because of the limited number of samples manufactured. This allowed extraction of the maximum amount of data from each tested sample.

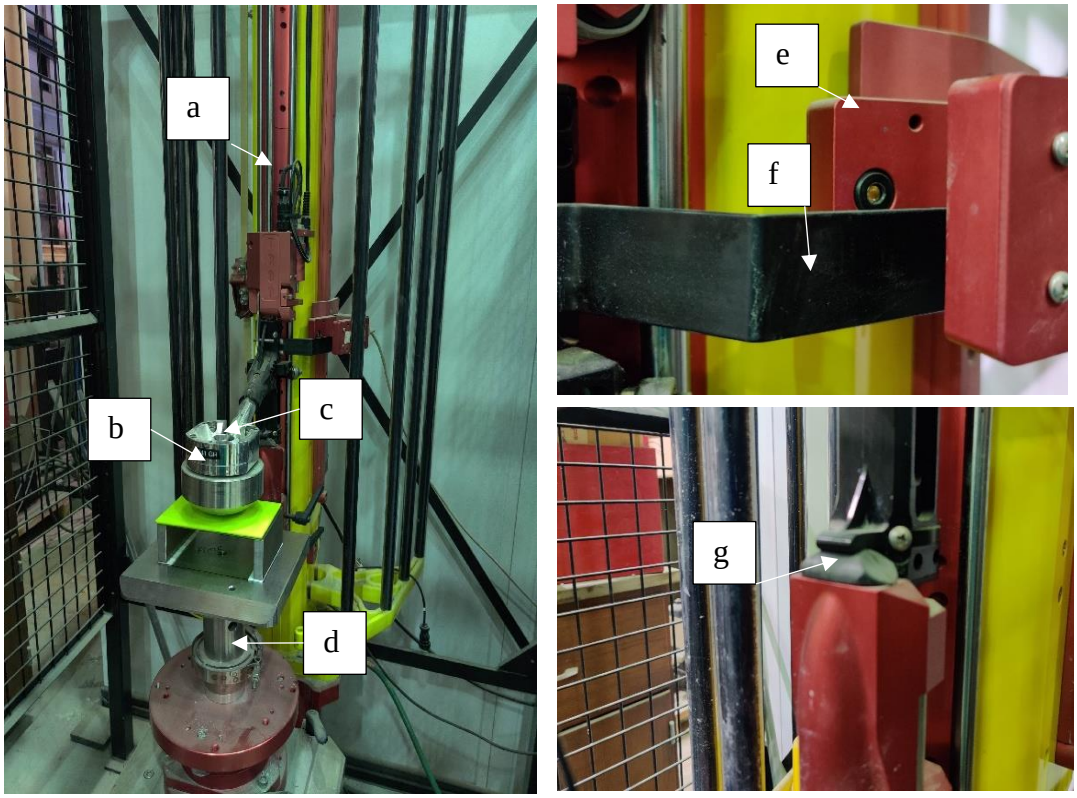

Figure 3.2 Drop tower components: (a) rail, (b) drop head, (c) accelerometer, (d) anvil, (e) time gate, (f) flyer, and (g) stopper.

3.3 Data analysis procedure

By integrating A, speed and position of the head during impact was obtained. However, due to lack of ability to pinpoint the end of the impact or failure of the sample on the acceleration curve alone, those curves were judged to be imprecise and not significant enough for a deeper analysis. Instead, the deformation of the sample was modeled using a simply supported beam assumption [2] in order to derive two main parameters from A and P. The beam's stiffness k_B (in $N.m^2$) [Eq. 1], which correlates to the sample's resistance to deformation where is P is the load. The d is the distance between the two support, and δ_{mid} is the vertical displacement of the center point of the sample. The maximum strain energy density inside the sample U_{max} (J cm^{-3}) [Eq. 2] correlates to the energy absorbed during the impact with κ_{max}, the maximum curvature of the sample. M_{max} is the maximum moment generated by the deformation, and A is the acceleration of the impactor (see Appendix 5 for details). This model was used because it provided a quicker and less complex data analysis tool compared to models that are more accurate. The equations being simple guaranteed that everything could be done by an accessible software like Excel. Efficiency was very important considering the amount of data to process and the relatively small amount time dedicated to this project.

$$k_B = \frac{Pd^3}{48\delta_{mid}} \tag{1}$$

$$U_{max} = \frac{\kappa_{max} M_{max}}{2A} \tag{2}$$

Using the beam model, curves depicting the variations of both k_B and $Umax$ as a function of time can be obtained since the software records all the information needed

every 0.003 ms. The slope of the k_B curve correlated to the damage accumulation rate so they can be used to determine if peening can reduce the amount of damage generated at each drop.

3.4 Results and discussion

The main parameters taking in consideration for the analysis are the height of the last drop where the sample cracked and the variations of stiffness and strain energy densities with increasing drop height.

3.4.1 Drop height at failure

The height of the last drop (h_{max}) will indicate if a sample is failing prematurely relating to poor damage accumulation resistance. Looking at the average drop height at break (Figure 3.3), it is noticeable that most samples failed in the 50 cm to 55 cm region. Only two patterns seem to be underperforming here, namely L3-3X-S4 and L1-3X-S7. Even with the standard deviations taken into account, L1-3X-S7 is still standing out as the worst pattern in terms of damage accumulation resistance. The highlighted patterns are both “bottom stacked” types, meaning most of the LSP treatment is applied at the bottom of the sample (facing the support).

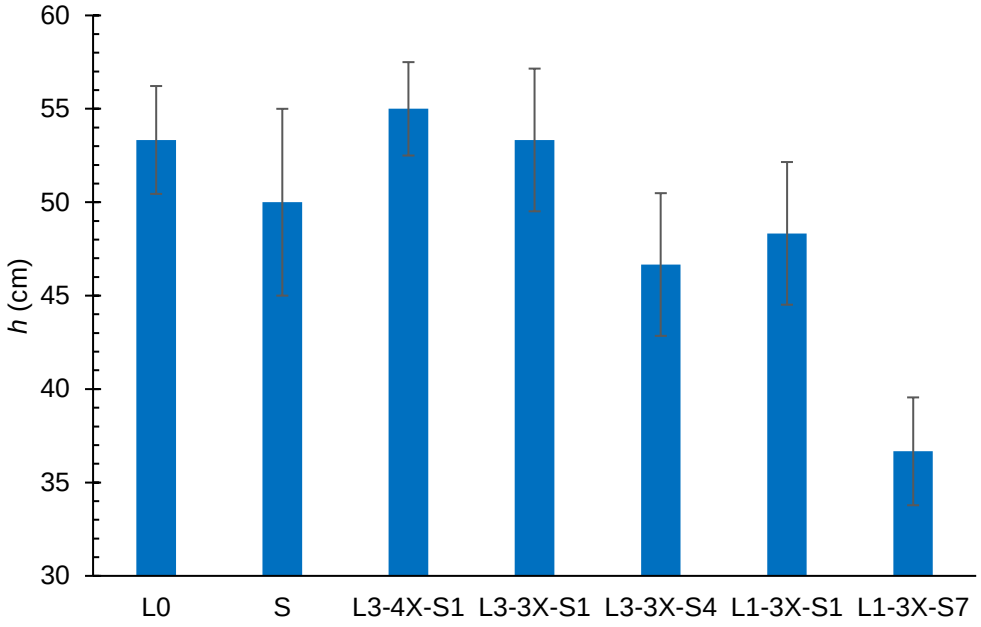

Figure 3.3 Average h_{max} for each pattern.

3.4.2 Stiffness variations with increasing drop height

A loss of stiffness is a loss in mechanical property as an indicator of damage accumulation. It is directly connected to the accumulation of micro-cracks inside the sample and potentially delamination [3] (in our case maybe separation of the layers). Taking a look at the average stiffness values for low damage (Figure 3.4a), most samples were within the 2.20 N.m^2 to 2.50 N.m^2 range. The unpeened (L0) samples have the second highest stiffness on average at 2.54 N.m^2 with the highest average stiffness belonging to the L3-4X-S1 pattern at 2.56 N.m^2. The lowest average stiffness was related to the S pattern that only had 2.24 N.m^2. Thus, it seems like LSP will not instantaneously increase or decrease the stiffness of the material based on number of treated layers. Additionally, the variation of stiffness for all samples were within the 10% range compared to the value of L0. Considering we converted data from the drop tower where the precision of the data is unknown, these variations are still significant but should be considered carefully. If we compare L3-3X-S1 and L3-3X-S4, the pattern

with the treatment stacked at the bottom of the sample had a higher stiffness. The same thing was not observable when comparing L1-3X-S1 and L1-3X-S7. The stiffness values at break (Figure 3.4b) also showed that the maximum damage accumulation always lowered the stiffness to a similar value for all patterns at approximately 2.0 N/m^2. This indicates that despite the high dispersity of some values, the test was mostly reliable.

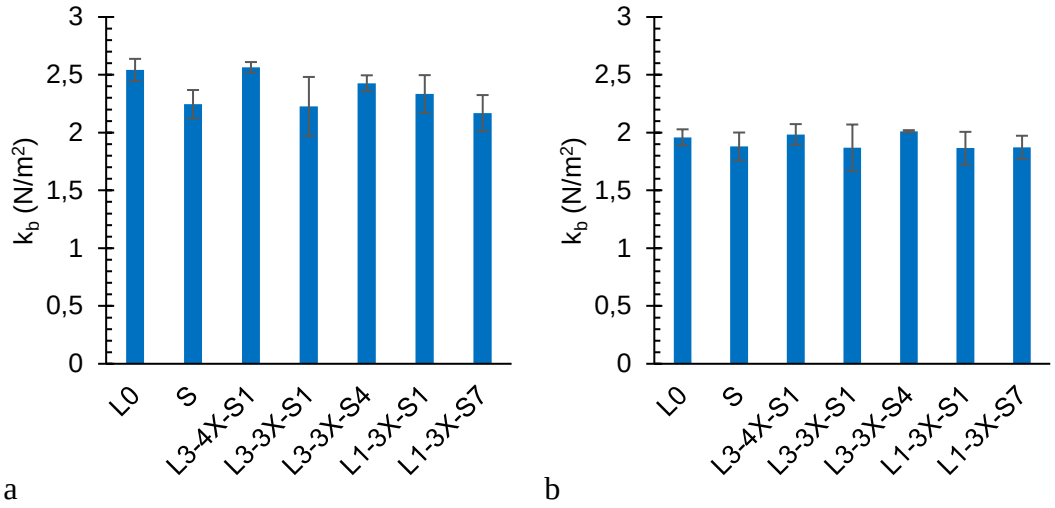

Figure 3.4 Average stiffness values: (a) at h = 10 cm and (b) at $h = h_{max\text{-}1}$.

In order to understand why some patterns are reaching failure earlier, even if the instantaneous stiffness was not noticeably affected, the variation of stiffness with the increasing impact height was plotted for each sample in Figure 3.5.

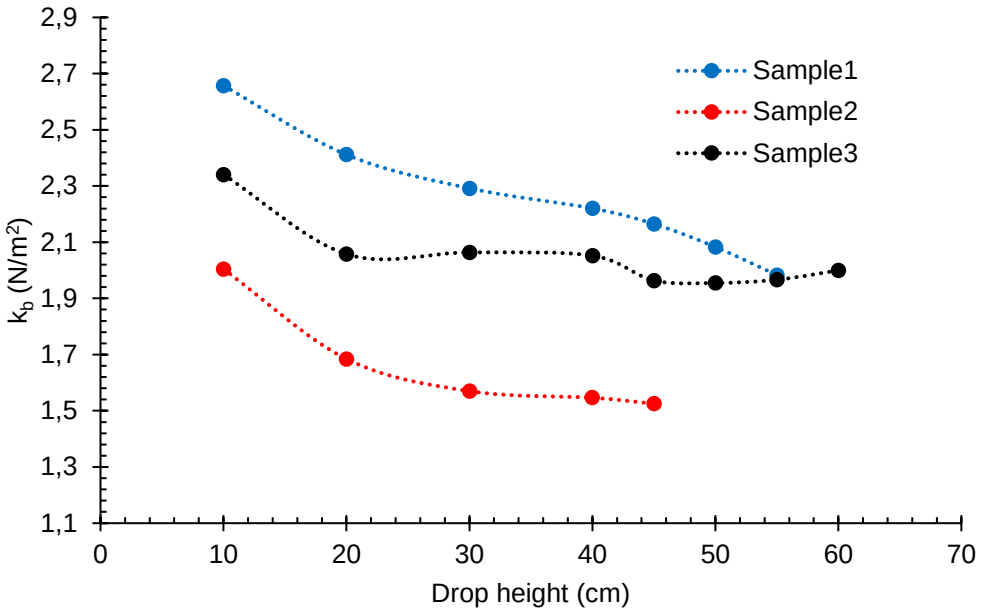

Figure 3.5 Variation of stiffness with increasing drop height for L1-3X-S1.

The slopes of these curves indicates the rate at which the samples are accumulating damage. To simplify the intense data processing, it was decided to base the slopes of all the curves by a linear model. However, looking at Figure 3.5, it is clear that certain parts of the curves are shaped more like exponential functions. A batch of identical samples could have been useful to determine if a better model than linear could have been chosen but the lack of time and resources did not allow this kind of study for this work. Hence, using a linear model, Figure 3.6 shows that L1-3X-S7 type samples are losing stiffness faster than the other patterns that all have similar damage accumulation rates considering some have huge standard deviations. This correlates well to the previous observations meaning stacking treatment at the opposite side to the impacted surface seems to increase your damage accumulation rate resulting in less durability against repeated impacts. The L3-4X-S1 type samples also had relatively high damage accumulation rate compared to the other patterns. Considering the L3-4X-S1 type samples also have the highest h_{max} out of all samples, it seems like the

distribution of treated layers helps the samples keep their integrity even with high damage accumulation.

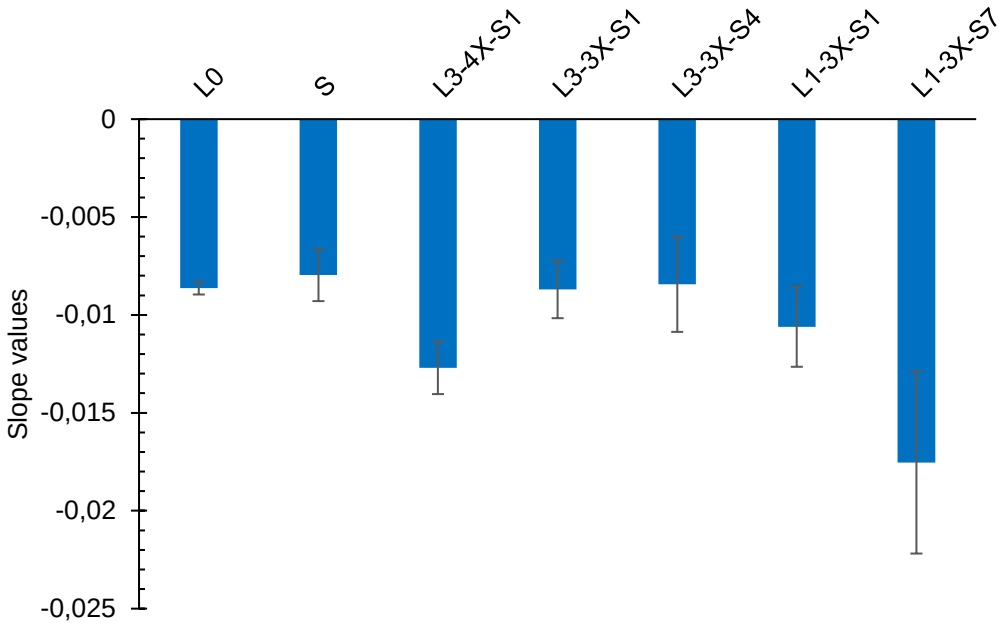

Figure 3.6 Damage accumulation rates for each pattern.

3.4.3 Strain energy density at break

Strain energy density corresponds to the amount of energy related to sample failure. During the impacts, small cracks are generated within the sample. It is the amount of energy related to the apparition of those cracks that is measured. At complete failure of the sample, the strain energy density corresponds to the amount of energy necessary to break the sample apart. As it is, L3-4X-S1 seems to be the best pattern for energy absorption and L3-3X-S4 and L1-3X-S7 seem to be the worst. This could mean that even at maximum damage accumulation, samples are not equivalent to one another with some samples at their limit in terms of absorption while others could have taken more damage given a lesser intensity impact.

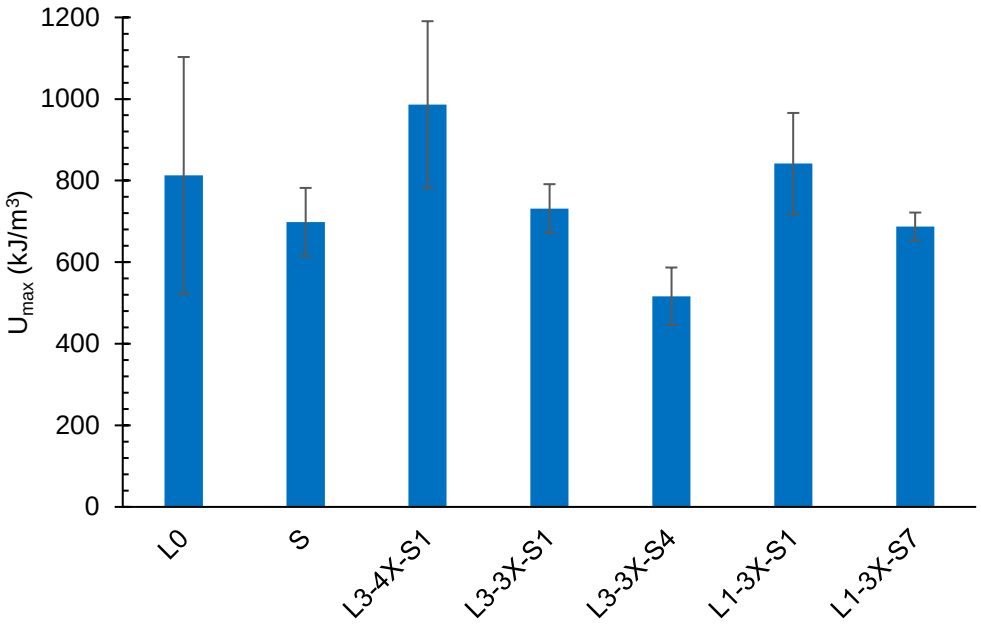

Figure 3.7 Average maximum strain energy density at break.

Moreover, the average U_{max} at break can be correlated to the average h_{max} for each pattern type since they both show a similar trend represented in Figure 3.8a and Figure 3.8b, respectively. Looking at the red line, it is observable that mostly a higher energy absorbed at break translates to a better durability of the sample (described by a higher h_{max}). This makes sense on a mechanical standpoint since it means that more energy is necessary to reach failure for more durable samples. It can be noted that L3-3X-S4 and L1-3X-S7 are underperforming in this domain and so is S. The impact of each individual peened layers is hard to observe on a test like this and needs further investigation.

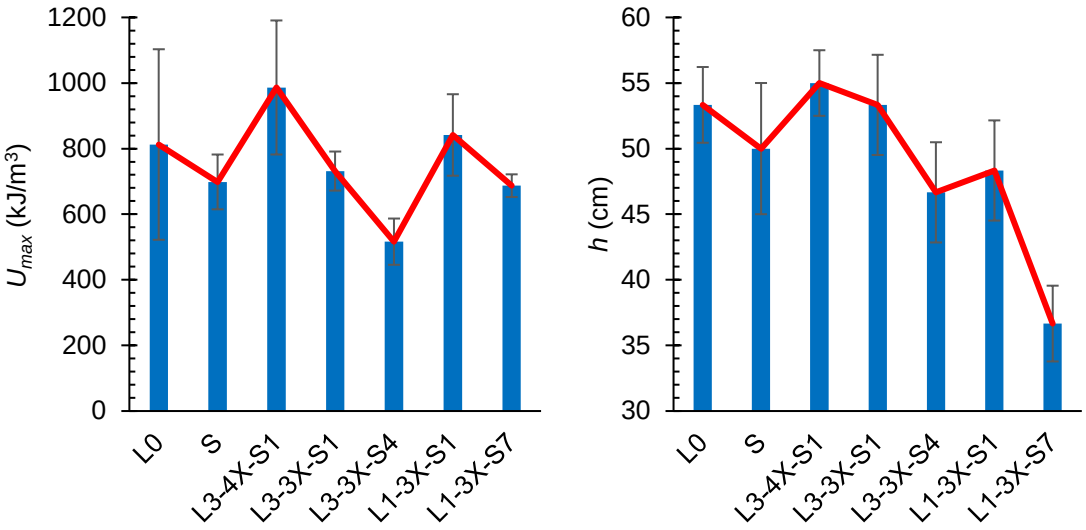

Figure 3.8 (a) Average U_{max} at break trend and (b) average h_{max} trend.

3.5 Heavier delamination of samples

In some cases, very noticeable delamination was observed at sample failure. For instance, all L3-3X-S1 samples suffered from heavy layer separation illustrated in Figure 3.9, where all the individual layers were visible instead of having a failure line that cuts the sample purely vertically. Delamination most likely happens at a micro level for all samples but for the ones where it is very noticeable like L3-3X-S1, it could be due to the regular contact with water with insufficient drying time that affected the layer-to-layer adhesion in the sample. It is unsure what kind of impact this phenomenon has on the samples stiffness, damage accumulation rate, or resilience since L3-3X-S1 samples have average performances in these areas compared to the other samples.

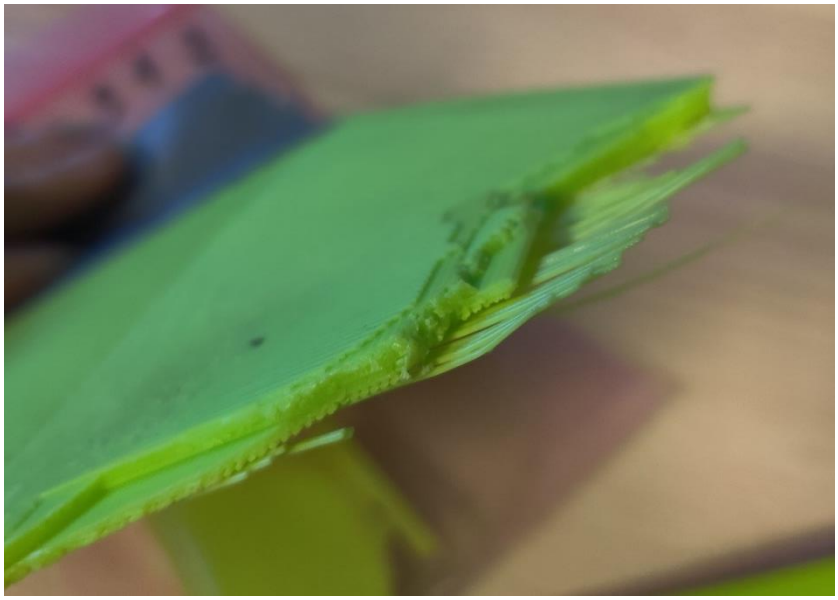

Figure 3.9 Observable layer separation on L3-3X-S1 sample

3.6 Summary and Conclusions

The hybrid manufacturing method seems to impact the mechanical properties like stiffness. However, this influence is unpredictable with the analysis of the current results since no trend was found for the increase of stiffness related to the number of treated layers or the distribution of said layers within the material. The impact of peening was more noticeable on damage accumulation with a few trends appearing. First, samples from the L3-4X-S1 pattern had the highest average h_{max} with good reproducibility as well as the highest average stiffness values overall. Then, L1-3X-S7 and L3-3X-S4 patterns had the lowest U_{max} at break as well as the lowest average h_{max}. L1-3X-S7 samples also have the fastest damage accumulation rates. All these elements suggest that in an impact resistance test, having the greatest number of peened layers is beneficial. On the contrary, stacking the peened layers on the bottom of the sample was not a good option. This could be due to LSP increasing the stiffness of each individual layer since the stiffness increase in the material is less elastic. The bottom layers were put under more stress. If all the bottom layers are stiff, they might crack more easily,

and the damage will propagate faster contrary to having more elastic bottom layers that can withstand the deformation. That would explain why L3-3X-S1 and L1-3X-S1 have good h_{max} and U_{max} at break values. L3-4X-S1 being a more balanced distribution might not suffer from this phenomenon since there is no difference of stiffness between the top and bottom half of the samples. We can also notice a similar trend between the strain energy densities at break and the average maximum impact height. In order to confirm the role of each peened layer in the resistance to deformation, a test on a slower scale needs to be performed. This last point will be investigated in future work using a three-point bending set-up.

CHAPTER 4

VISCOELASTIC BEHAVIOR

4.1 Introduction

Dynamic mechanical analysis (DMA) is often performed on polymers or polymer-based composites to study the degradation or aging effects of certain uses or environments. For instance, mechanical property loss in polymers due to aggressive or corrosive environments [1,2] can utilize DMA to characterize viscoelastic properties. DMA can also be used to predict the behavior of viscoelastic materials exposed to repetitive mechanical stress at high frequencies using the time-temperature superposition principle. Although studies have shown that it is possible to elaborate new DMA techniques to study high frequencies mechanical deformations directly [3]. In this case, DMA was performed in order to study the viscoelastic behavior and relaxation properties of peened samples. This test also gives us some information about the glass transition and crystallization phenomenon by estimating the temperatures at which they happen. Even though a differential scanning calorimetry (DSC) is usually preferred for analyzing these two parameters, the lack of time did not allow for other testing methods. So, the DMA acted as a multifunction test but less accurate in some domains. For instance, the manufacturer of the PLA filament PolyLite^{TM} used DSC to determine the glass transition, crystallization, and melting temperatures shown in Table 4.1.

Table 4.1 Significant temperatures of PLA filament [4]

Property	Testing Method	Typical Value
Glass transition temperature	DSC, 10°C/min	61 °C
Melting temperature	DSC, 10°C/min	150 °C
Crystallization temperature	DSC, 10°C/min	113.5 °C

4.2 Materials and Methods

The machine used was a DMA 850 with an ACS-2 compressed air cooling system both manufactured by TA Instruments®. The air-cooling system was preferred to a traditional hydrogen cooling system for its ease to set-up and the lack of usage of hydrogen tanks, creating both a safer and more reliable environment.

Samples were cut from the plates used during the impact tests due to the inability to make more peened samples. The sample geometry was a prism of dimensions 35 mm × 10 mm × 4 mm as shown in Figure 4.1. The length of 35 mm was based on the distance between two clamps (one being the mobile clamp using a cantilever set-up) inside the DMA machine with 5 mm extra to ease the set-up. The width of 10 mm was standard for DMA samples with this machine.

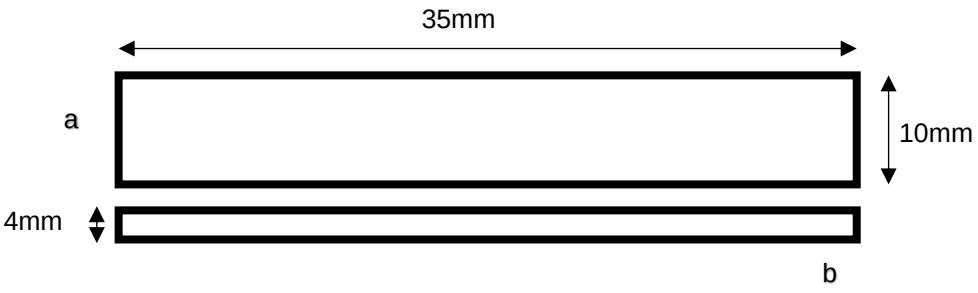

Figure 4.1 Geometry of DMA sample: (a) bottom view and (b) front view.

The test was performed in a cantilever set-up at a frequency of 1 Hz. The linear temperature ramp was set-up between the coldest temperature the machine can reach at -55°C and 120°C at a temperature below the melting point of the material since the goal was only to study the relaxation phenomenon. The temperature increased at 2 K/min to ensure a slow and steady heating of the sample. Two samples were tested for each pattern. Both samples for each pattern were cut from the same plate and the same region of every plate to minimize the potential fluctuations in sample quality. All results are averages obtained from both samples. The samples were cut using a circular saw blade and refined using sandpaper. Please refer to Figure 2.1 for nomenclature of the samples.

4.3 Results and Discussion

The results will be drawn from the temperature dependencies of the storage (elastic) modulus E'(T) associated with the rigidity of the material; the loss (viscous) modulus E"(T) associated with the toughness of the material; and the damping factor tan δ(T) curve which is given by:

$$\tan(\delta) = \frac{Storage\ modulus}{Elastic\ modulus}$$

All three parameters were studied based on their temperature dependence.

4.3.1 Glass transition & Material relaxation

Figure 4.2 shows the average loss modulus variation with temperature for all patterns. The peak of the loss modulus curves is a manifestation of the α relaxation during which the material is dissipating energy. A higher loss modulus value indicated higher dissipation properties for the material. Figure 4.3 shows the maximum loss modulus values for all samples. It was observed that by applying peening, this value increased compared to L0. Hence, by applying LSP to the material, the energy

dissipation properties of the material were improved. Considering the margin of error and standard deviation on these values, the pattern that stands out seems to be L3-3X-S4 even though its modulus was comparable to S and L3-4X-S1. Looking at the average values for L1-3X-S1 and L1-3X-S7, it seemed that spreading out the peened layers was more beneficial for dissipation properties. The case of L3-3X-S1 also exhibited a lower average maximum modulus. This was likely associated to delamination observed after the impact tests on all L3-3X-S1 samples. Even if the samples were taken from parts with no visible delamination, the decrease in layer cohesion might have affected the samples in a manner not perceivable to the eye.

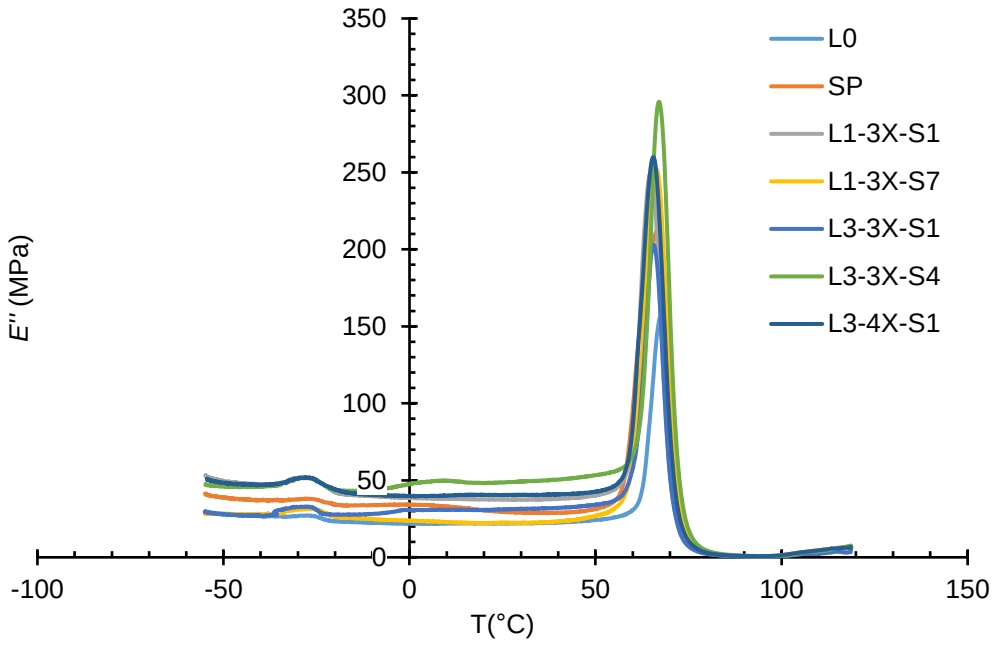

Figure 4.2 Average loss modulus variation with temperature.

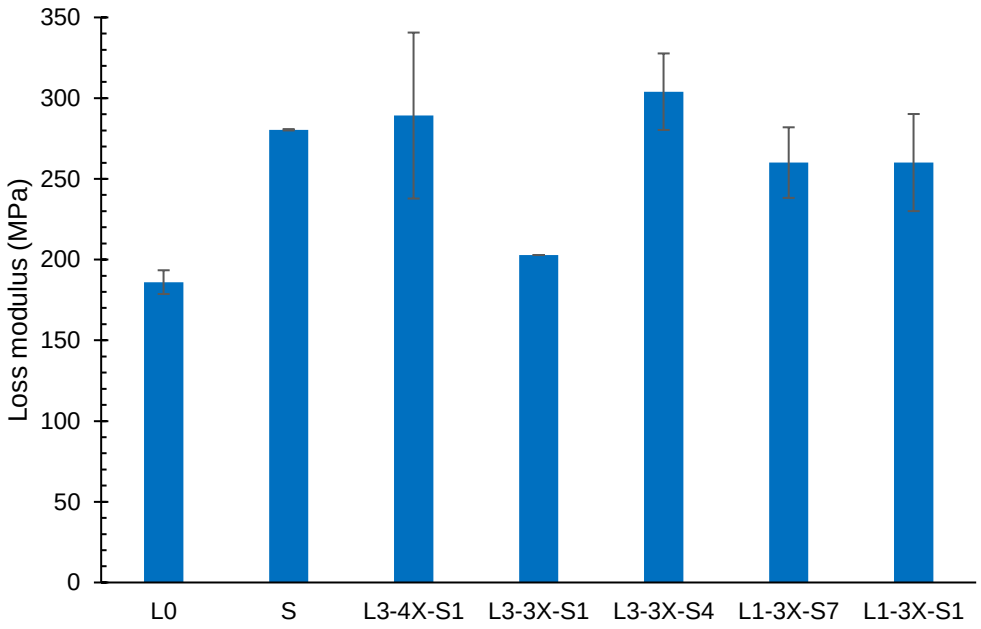

Figure 4.3 Maximum loss modulus.

4.3.2 Stiffness variations

The elastic modulus is a reflection of the rigidity of the material, which usually means the higher the modulus the higher the stiffness of the material [2]. Figure 4.4 shows the average variation of storage modulus for all the patterns. The glass transition has been established between 68°C and 64°C for all samples. Under this range of temperatures, the material is in the glassy state. Comparing the *E'* values for all samples at 20°C (Figure 4.5), it was obvious that some patterns had higher storage modulus values. L0 had the second lowest at 1.2 GPa, which might indicate an increase of stiffness due to LSP. This is feasible since LSP induced compressive residual stress is supposed to increase mechanical properties such as tensile strength. The noticeable trend was higher storage moduli for patterns where the peening was stacked at the bottom of the sample, namely L3-3X-S4 at 1.70 ± 0.03 GPa and L1-3X-S7 at 1.60 ± 0.10 GPa. Other patterns that performed well were the ones with both top and

bottom layers treated with S type and L3-4X-S1. However, it should be noted that L3-4X-S1's average modulus was approximately 0.1 GPa higher than the S type despite having two more peened layers and was lower than L3-3X-S4 with one more peened layer. Since a cantilever configuration was used, there should be no difference between similar patterns but upside down like L1-3X-S1 and L1-3X-S7. Hence, the difference in behavior must come from a different internal cohesion between the samples from each pattern. Therefore, these observations suggest that spreading out the peened layers was more efficient most likely for sample cohesion reasons. Again L3-3X-S1 can be put aside due to the previously mentioned delamination issues with those samples. The trend of values for each pattern was similar to the one seen with maximum loss moduli. There seemed to be a correlation between these parameters. By applying LSP, it was possible to improve both the stiffness and the dissipation properties of the material in this type of loading.

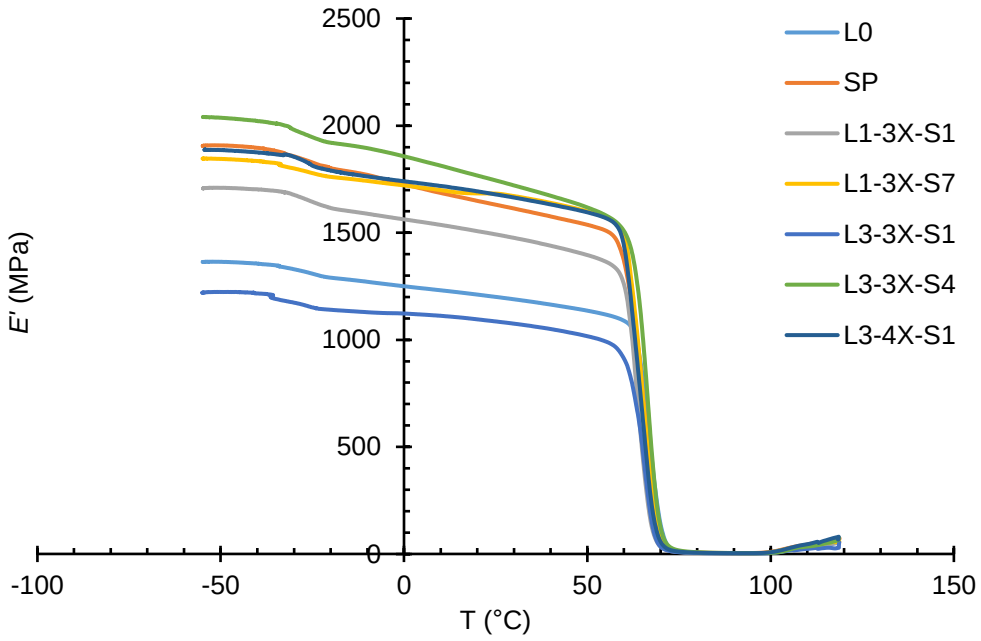

Figure 4.4 Average variation of storage modulus for each pattern.

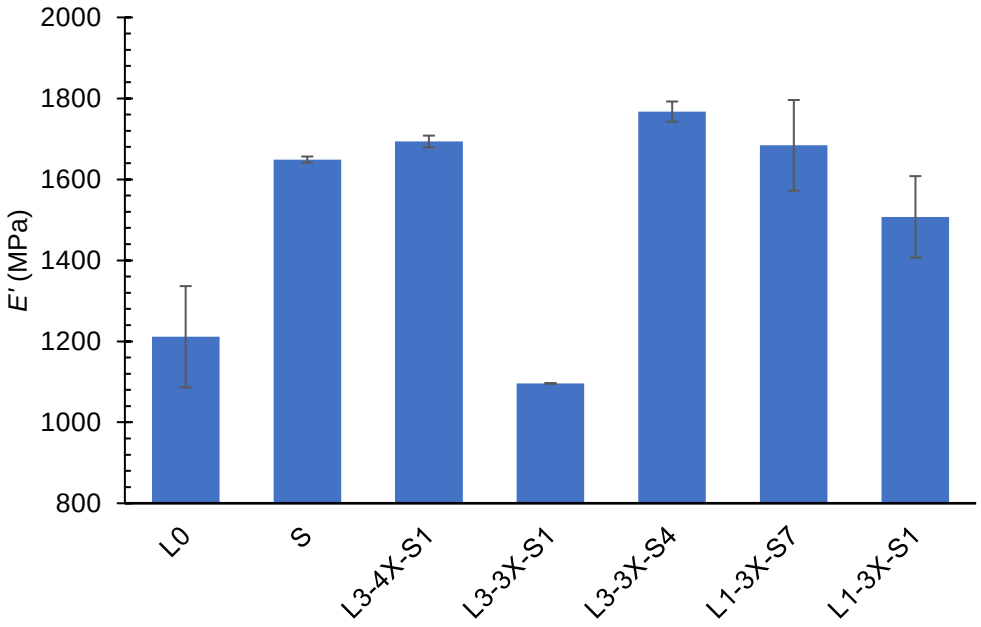

Figure 4.5 Storage modulus at 20°C.

4.3.3 Cold crystallization

After 80°C, both *E'* and *E''* curves were going from a stiff drop to an upward trend all the way until the cut off temperature at 120°C as shown in Figure 4.6 (it does not make much difference if we look at *E''* or *E'* curves). A logarithmic scale was used to better highlight the variations of moduli around the cold crystallization region. This dip followed by a rapid increase was the signature of cold crystallization [7]. The bottom of the dip can be approximately associated to the start of crystallization inside the material. The minimum value for *E'* varied between 2.6 MPa and 3.6 MPa across all samples. If a point was taken in the crystallization region arbitrarily at *E'* = 10 MPa, the temperature varied from 100°C to 103°C in the same way at *E''* = 2 MPa where the crystallization temperatures were between 102°C and 106°C. These variations were not significant enough to ensure that LSP influenced the cold crystallization process.

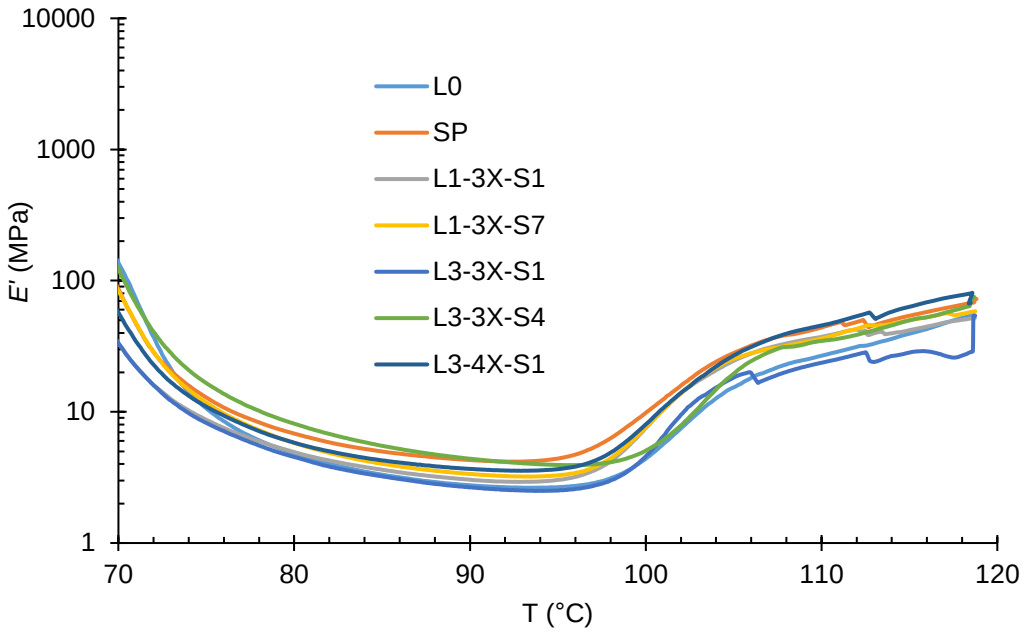

Figure 4.6 Variation of storage modulus around the cold crystallization region.

4.4 Summary and Conclusions

The α relaxation seems to be impacted slightly by LSP. Stiffness and energy dissipation properties of the material were both globally increased after LSP with L3-3X-S4, L3-4X-S1, and SP patterns with the highest increase compared to L0. In the case of small elastic solicitations, the way to maximize the benefits seemed to be spreading out the peened layers. However, differences in behavior were observed between top stacking and bottom stacking the treatment, which should not be the case for a cantilever set-up. It is possible that other factors, such as sample quality of layer to layer cohesion effects, are also responsible for those results. The storage modulus after 80°C was not heavily impacted by LSP. Hence, the induced compressive residual stress does not seem to hinder the crystallization rate nor create favorable nucleation sites. This could also be confirmed through DSC or microscopic observation during crystallization.

It should be noted that the stiffness values and trends across the patterns did not correlate well to the results observed in Chapter 2. This is mostly due to the nature of the tests being different. In the case of DMA, the material was tested in the elastic region on very small deviations whereas the impact tests were on a bigger scale with instantaneous deformation.

CHAPTER 5

CRACK PROPAGATION AND DEFORMATION

5.1 Introduction

This test will allow for a characterization of the effects of peening on the resistance to deformation in a similar manner to the impact resistance test mentioned in Chapter 3. The primary difference is testing on a much slower and localized scale which allows for a more detailed description of the behavior of individual layers. The work described in this chapter was done in partnership with the laboratory of INSA Rouen to understand crack growth behavior in hybrid additive manufacturing of polymers.

5.2 Materials and Methods

A standard three-point bending test based on ASTM 1820-21 norm [1] was performed using an MTS 810 servo-hydraulic testing machine. The displacement was 5 mm/min until gradually overloading the sample and recording the load (P in kN) and vertical displacement (d in mm) values. The piston pulled the sample in the tool until the sample cracked to a satisfying degree, meaning low enough resistance for the operator to consider the response is fully plastic (typically when the force starts to stabilize at low values or reaches 0). The sample was placed between two cylindrical supports with a gap of 45 mm.

Two sample geometries were studied with one referred to as “flat” or designated by “F” and a seconed one called “edge” or designated by “E” (Figure 5.1). Both were shaped like a rectangular prism of same dimensions 55 mm x 10 mm x 4 mm. Three

samples of each peening pattern were cutout using a water-jetting device for its higher precision. All samples were cut from a plate used during the impact testing (Refer to Chapter 3). This choice was made due to the inability to make more peened samples at the GPM Lab in Rouen, France. This limitation was also the cause for the lack of some samples, namely:

- Only three S type samples were cut from the base plates due to the other plates being shattered in pieces that were too small to cut after the impact test. All S type samples were tested in the “E” position mentioned below (Figure 5.1).
- Within the six L1-3X-S1 samples cut from the base plates, only three were used since one of the samples showed bad layer cohesion visible after the cut. All three samples were tested in the “F” position.
- Most samples of a singular peening pattern are cut from the same plate with the exception of L3-3X-S1, which had three samples from plate 2 and three samples from plate 3.

To ensure proper crack initiation, all samples had a V-notch cut into them. The depth of the notch varied between sample geometry. One had 0.2 mm on the flat part facing away from the tool during testing for “F” type samples. The other had 1 mm on the edge of “E” type samples again facing away from the tool. The difference in notch size can be explained by the sample’s orientation. For “F” samples, the smallest notch was needed to ensure minimal loss of treated layers.

For E samples, the notch has to be deeper considering the difference of material amount in the testing orientation. Thus, 1 mm is enough to ensure smooth cracking. All notches were finished using a razor blade to minimize the surface at the bottom of the notch. In the E type samples, all layers were loaded relatively equally at a given time,

which means that any variation was most likely be due to the number of treated layers and not to the repartition of said layers inside the sample.

For F type samples, the loading direction was from the top and perpendicular to the layers and thus perpendicular to the induced CRS direction. Additionally, the bottom layers were loaded more than top layers. The effect of each individual layers or groups of layers might be more visible.

The samples described in this chapter will be referred to with a combination of their name, followed by the type (E or F) and their number which corresponds in which order they were tested. For example, the first flat type sample from the L0 batch was referred to as L0f1. Since E type were tested after F type, the first edge type sample from the L0 batch will be referred to as L0e4 since it was tested beforehand.

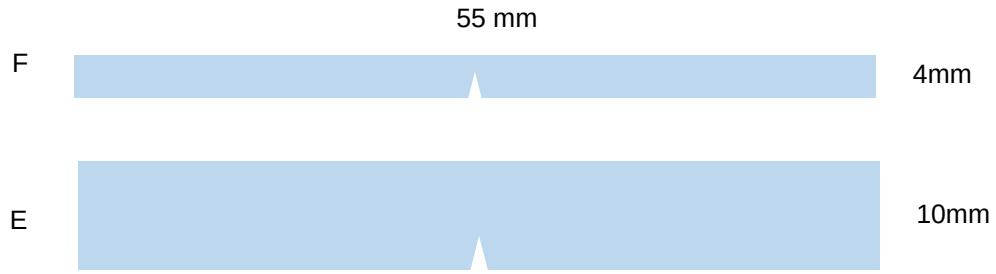

Figure 5.1 Three-point bending test samples: F is flat type and E is edge type.

Regarding crack propagation, a script developed by Dr.Vieille's team was used in order to process the data recorded by the three point bending equipment. The basic principles of the script will be discussed here. A camera recorded the deformation of the samples at a maximum rate of 24 frames per second. Every frame of the recording was binarized as described in Figure 5.2. The script then associated a point in time with its load and displacement values to a frame of the recording. With the binarized image, the script could distinguish the sample (in black) from the background (in white).

Hence, it recognized the edge of the notch in the sample (see Figure 5.1), which corresponded to the tip of the white shape in the middle of the sample. After providing information such as, the length, the thickness of the sample, the size of the notch, and the distance between the supports, the script was able to track the evolution of the crack that propagates through the sample.

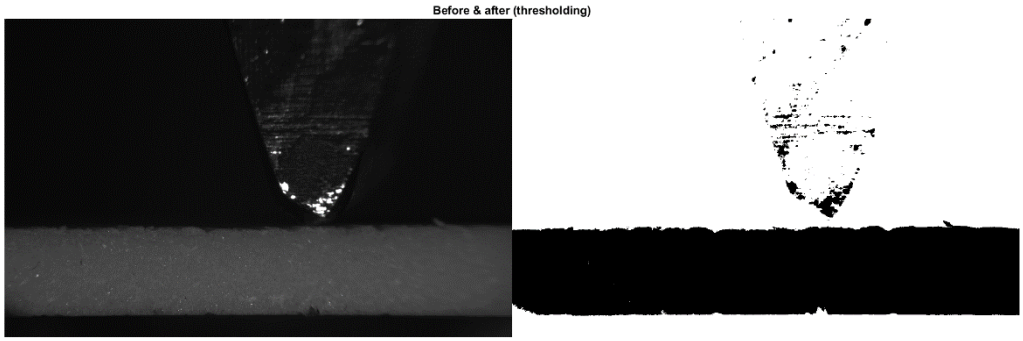

Figure 5.2 Original image versus binarized.

The script returned a lot of information, but this study will focus on two results: the x,y displacement of the tip of the crack also known as “crack path” and the “crack propagation,” which is the vertical displacement of the crack over time. This information combined with the recording of the samples gave a good idea of how the crack propagated through the different patterns. However, the script was quite sensitive with the amount of lighting on the test subjects and how the light was reflected by the sample. Some samples could not be exploited due to poor image quality. Others had incompatibility errors with the script that could not be resolved. Due to the inability to produce more samples, only a part of the total batch was analyzed. The samples that will not be discussed in this section are the following:

- L3-3X-S1e samples
- L1-3X-S1e samples

- L0f samples
- One out of the three L3-3X-S1f samples
- One out of the three L1-3X-S7f samples

Additionally, a bug that was discovered relatively late alters the length unit for the crack propagation graphs, especially with the F type samples. Since the origin of the issue could not be figured out, the length unit will not be taken too seriously in this analysis, and the shape of the curves will be the main source of interpretation.

5.3 Results and Discussion

Some results were obtained through data analysis techniques developed by Dr. Benoit Vieille and his associates. The intellectual property of which belongs to the laboratory of INSA Rouen. Only the basic principles of the analysis will be discussed here.

5.3.1 Three-point Bending Stress-Strain Response

The load-displacement curves (Figure 5.3) can be broken down into three regions: the loading phase, propagation region, and the cut-off region. In the loading phase, the material was still in the elastic region and the crack had not initiated yet. In the propagation region, the sample started to permanently deform, and the crack was propagating towards the tool. In the cut-off region, the sample reached a satisfying deformation, and the load was stabilizing towards zero. The force and displacement values were negative because loading pushed downward on the sample (in the direction of gravity). The crack did not propagate through the entirety of sample as the remaining uncracked parts of the PLA had relatively elastic behavior. Looking at the curves, all

samples from one pattern had similar slopes in the elastic region which indicates good reproducibility of the test and compensates for the small quantity of samples.

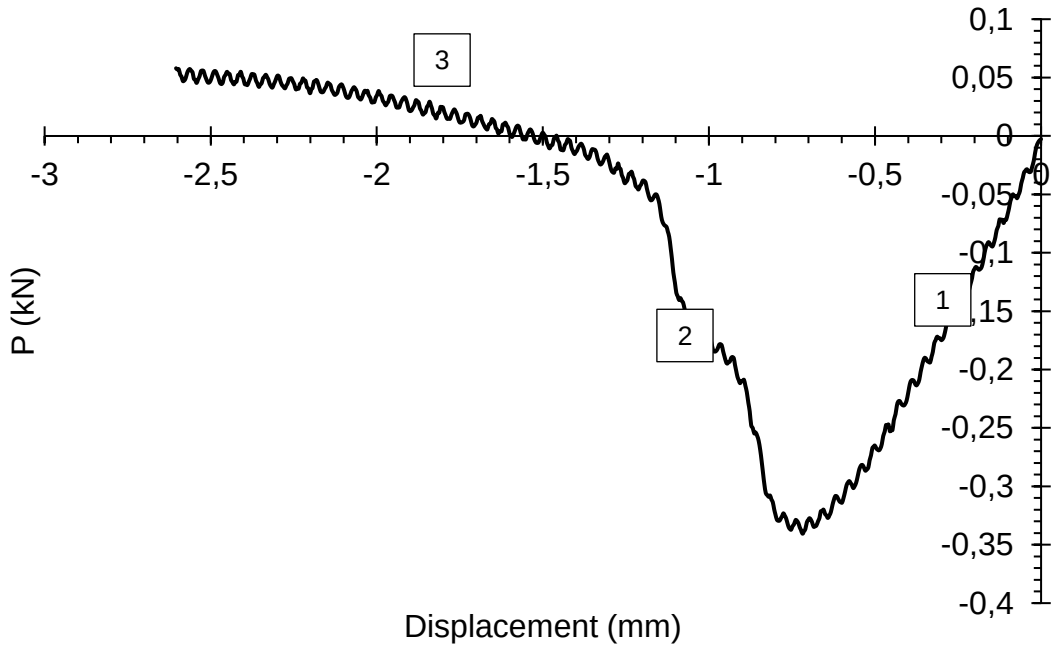

Figure 5.3 Example of load-displacement curve for L0 in E position sample: (1) loading phase, (2) propagation region, and (3) cut-off region.

Comparing the general shape of the curves between “E” and “F” samples, a clear difference was observable in the loading phase. In Figure 5.4, the comparison between the L0F and L0E samples showed that E type samples had a steeper loading phase, a higher maximum load applied, and reach the maximum load faster than the F type samples. This was due to the E type having more material in the direction of the applied force. Thus, samples were harder but broke faster compared to the F position that allowed for more elastic deformation.

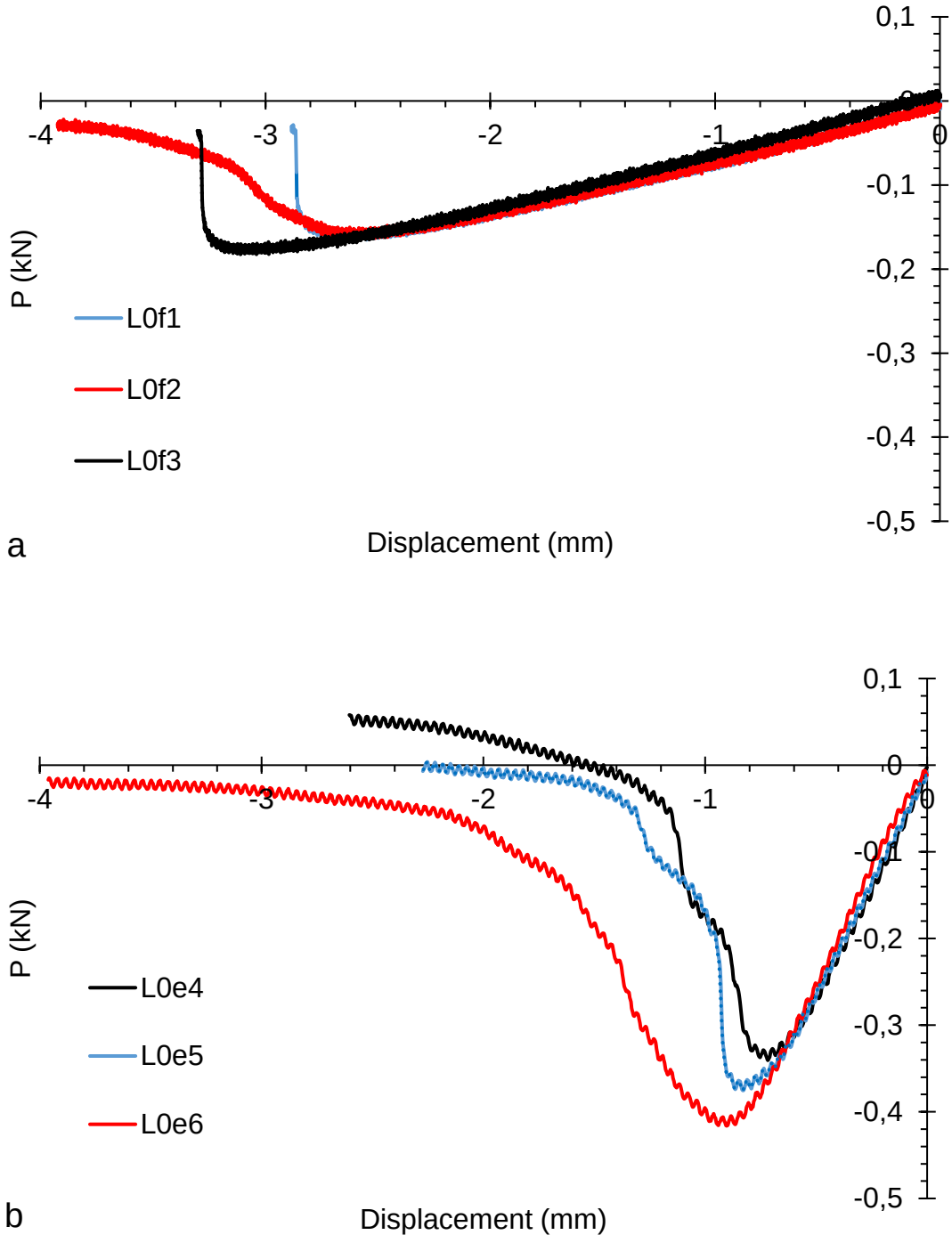

Figure 5.4 Load-displacement curves for all L0 samples: (a) F type L0 samples and (b) E type L0 samples.

The main parameters to focus on when looking at the load-displacement response are the maximum applied force which correlates to the plastic limit, the

displacement at maximum force which represents how much the sample deforms before tearing, and for E type samples, the slope of the elastic region which correlates to the toughness of the sample [2]. In the case of the F type samples, it did not make sense to look at the slope in the elastic region since the deformation was discontinuous (more details in 5.3.2 Crack propagation). At the lowest point of the curves, the average maximum force applied was given by Figure 5.5a and Figure 5.5b.

The values that are missing correspond to the samples that could not be tested due to the different issues mentioned previously. Here the goal was not to compare the values of E and F type samples directly but to compare the samples within them to figure out some kind of trend. In this regard, very similar trends were observed for maximum load applied where L3-4X-S1 and L3-3X-S4 samples had slightly higher values for both E and F types. Similarly, L0, L3-3X-S1, and L1-3X-S7 samples had comparable results for both E and F orientations. Looking at these results, despite lacking some samples it could be conjectured that the orientation of the sample will not highly affect the performances of a pattern relative to the others. However, the gap between patterns was still more noticeable in the E orientation, which is odd since all the layers are loaded at the same time. This could mean that LSP affected the properties of the sample not only in the direction of peening but also that the number of peened layers was not the only parameter affecting the performances of a sample. The general cohesion of the sample after being peened and impacted could have an important role in the performances of our material. The displacement at maximum force was also relatively stable across all samples except for L3-3X-S1, which seemed to stand out with a higher displacement with a similar amount of applied force compared to the other patterns.

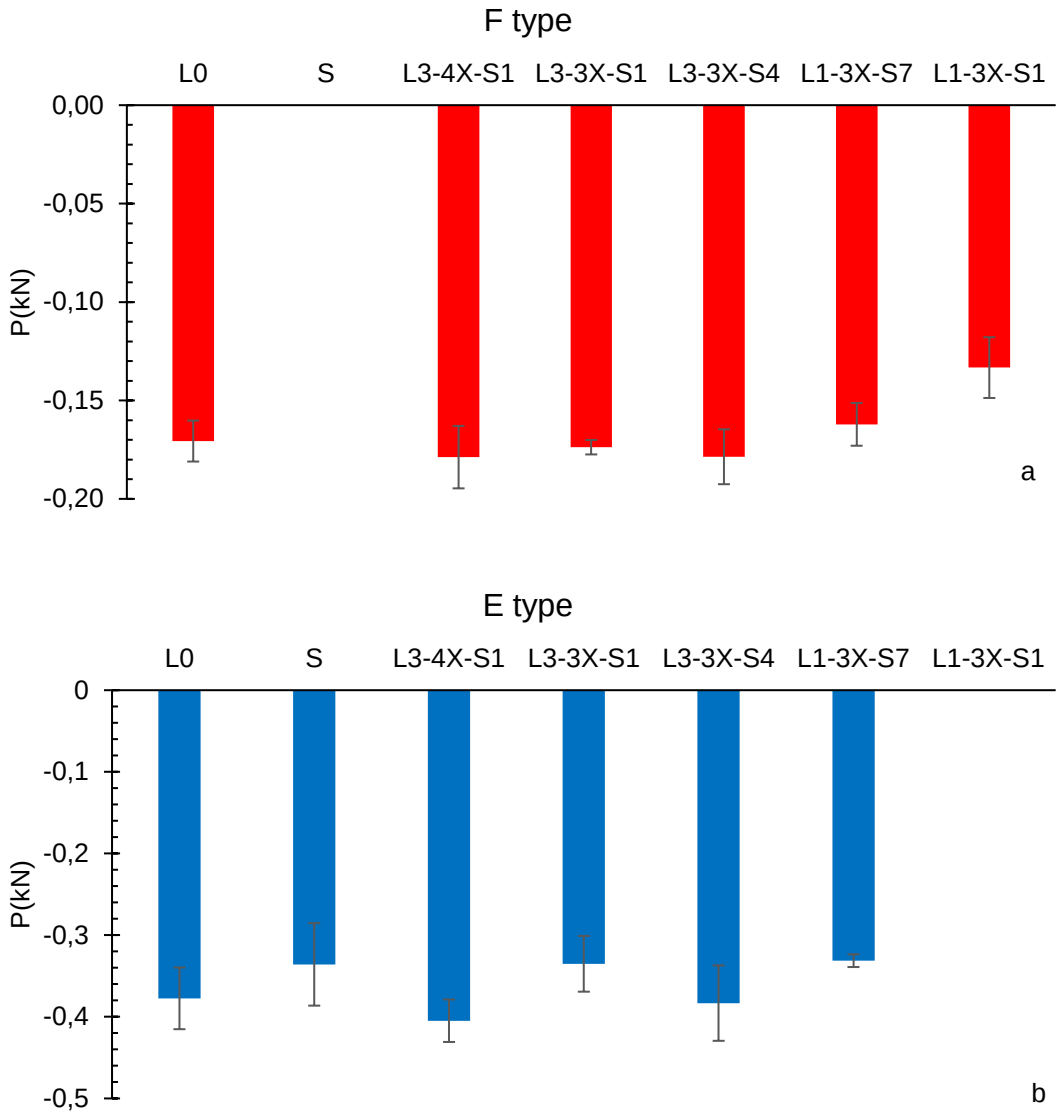

Figure 5.5 Average maximum load: (a) F type samples and (b) E type samples.

The average displacement at the maximum applied force for each pattern type are given by Figure 5.6a and Figure 5.6b. In this case, the trend from pattern to pattern do not look similar between the F and E type samples. For F type samples, the patterns that stand out are clearly L3-3X-S1 and L0 which have high displacement for a similar maximum load applied compared to the other patterns as observed in Figure 5.5. This indicated a lesser resistance to deformation. In other words, the samples were more

susceptible to bend under solicitation. Looking at Figure 5.6b, this behavior was also noticeable for L3-3X-S1 in the E orientation.

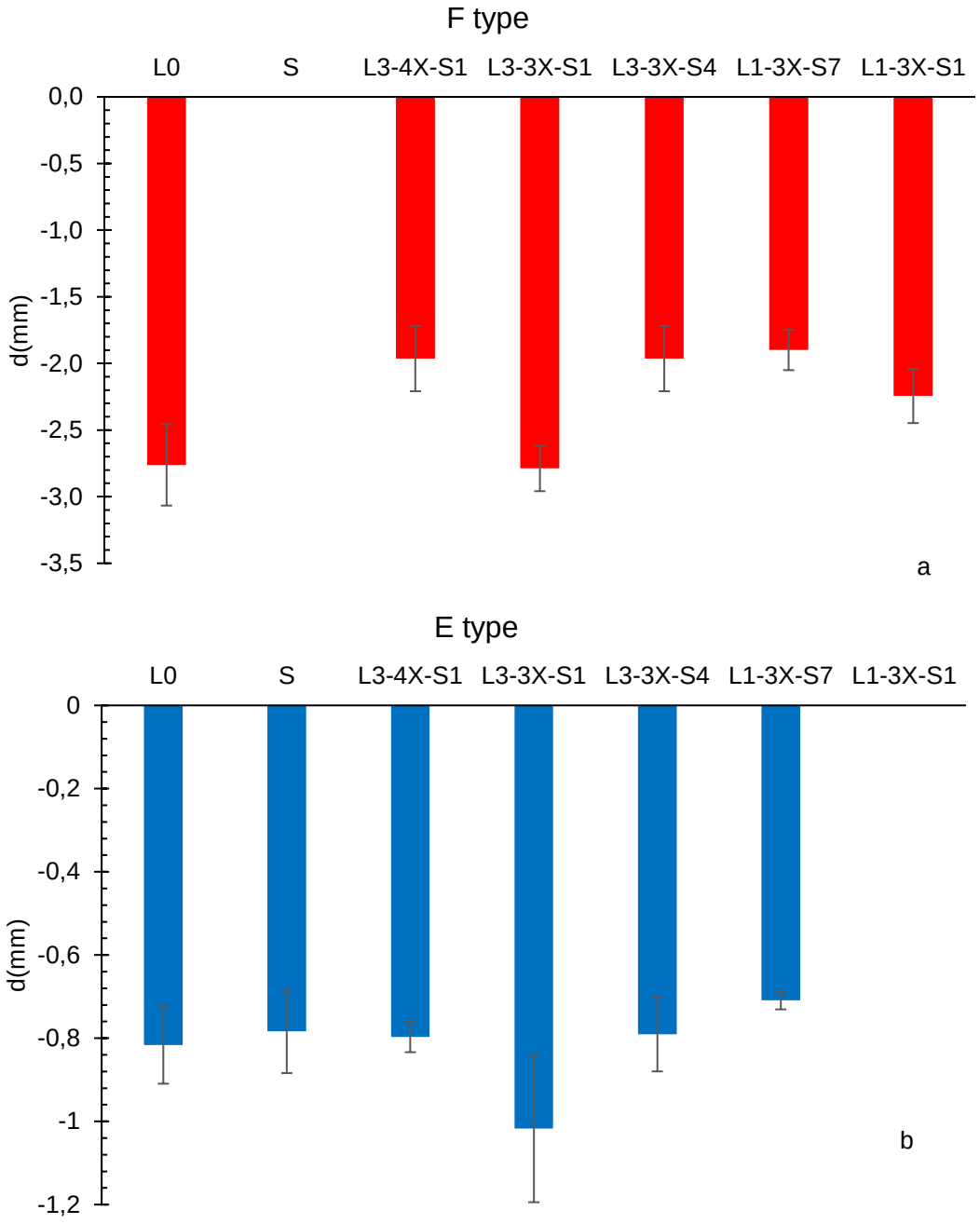

Figure 5.6 Average displacement at maximum load: (a) F type samples and (b) E type samples.

Combining this observation with the Figure 5.7, which shows the slope of the load-displacement curves in the elastic region for E orientation, correlates to the stiffness of the samples. It was confirmed that L3-3X-S1 was the most elastic pattern with the lowest average slopes. Actually, this can be explained by delamination of the L3-3X-S1 samples during the testing (Figure 3.9). Layers of the samples were not holding together resulting in less layers being loaded overall and thereby decreasing the mechanical properties of the samples. This delamination occurred during the impact resistance tests described in Chapter 3. It might indicate that the LSP process affected the layer cohesion of some samples like that discussed in Chapter 4. With this exception, the resistance to deformation seemed to be improved by the presence of LSP in the F orientation; however, no noticeable impact existed in the E orientation. This correlates well to the idea that the induced CRS was mostly effective against loading perpendicular to the stress's orientation.

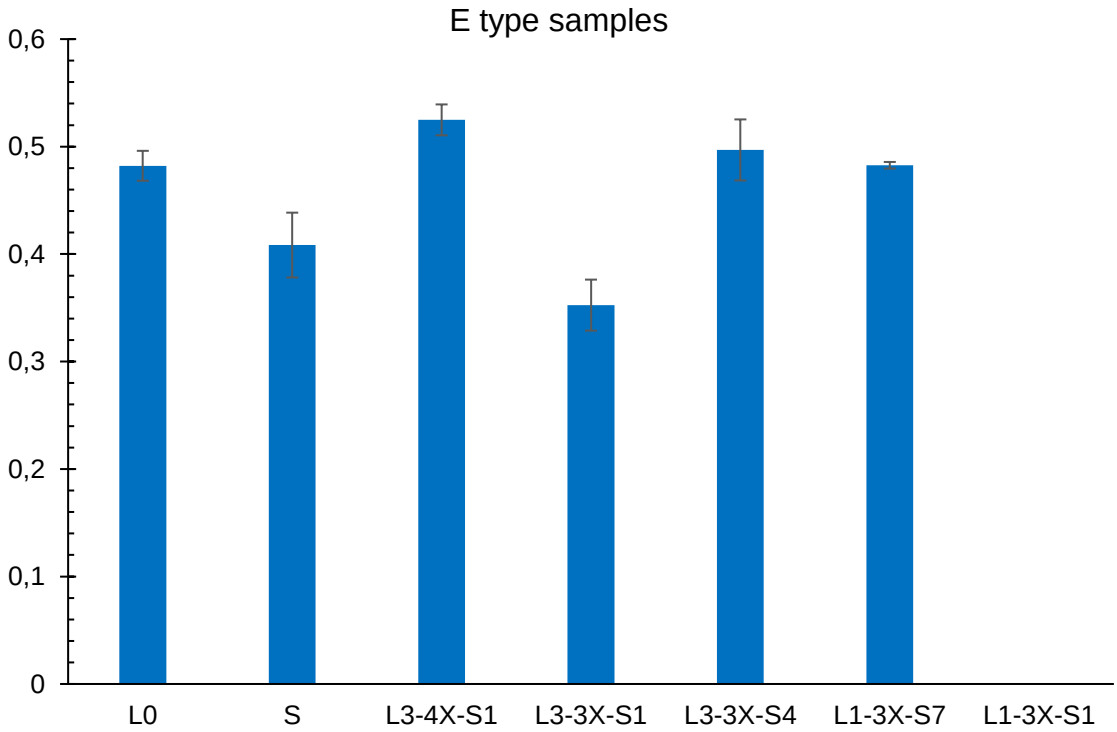

Figure 5.7 Slope values in the elastic region.

5.3.2 Crack Propagation

E type samples

The results for E type samples regarding crack propagation were very similar between most samples. Figure 5.8 shows a typical crack path for a sample in E position (in this example L1-3X-S7e4). The crack was very straight with small variations on the x-axis. The few exceptions that existed, where big variation were observed, are explained by notch identification problems from the script like for L3-4X-S1e4 shown in Figure 5.9. A side by side of the binarized start frame and end frame for this sample (Figure 5.10) reveals that the notch has extruding material on its side which messes with the script once the images are binarized, but the crack does propagate in a straight line.

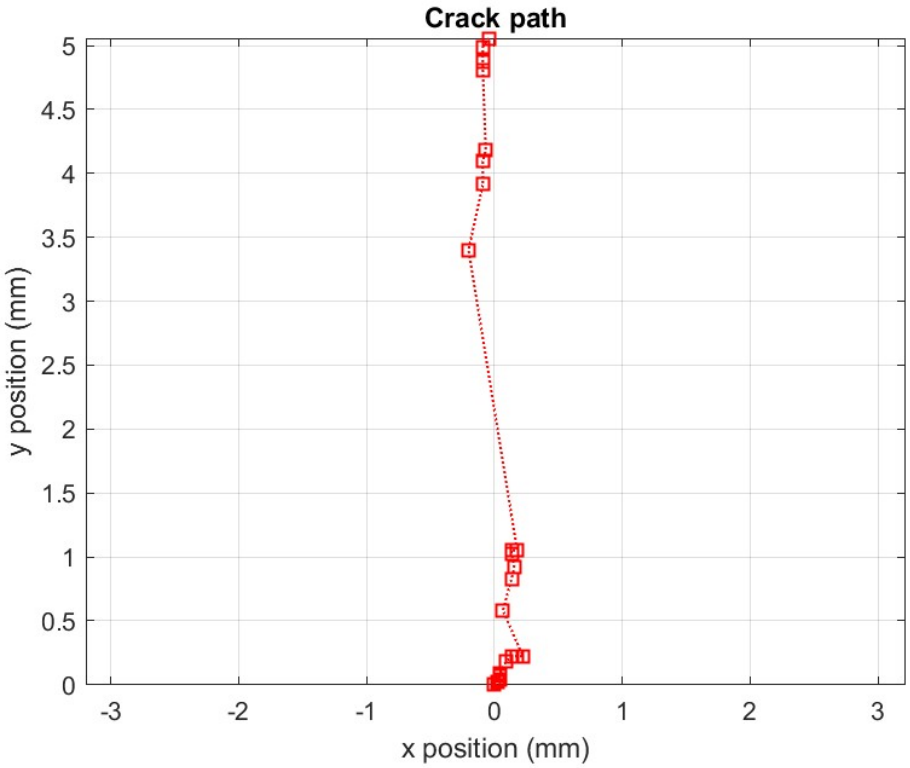

Figure 5.8 Typical crack path for E type samples (L1-3X-S7e4).

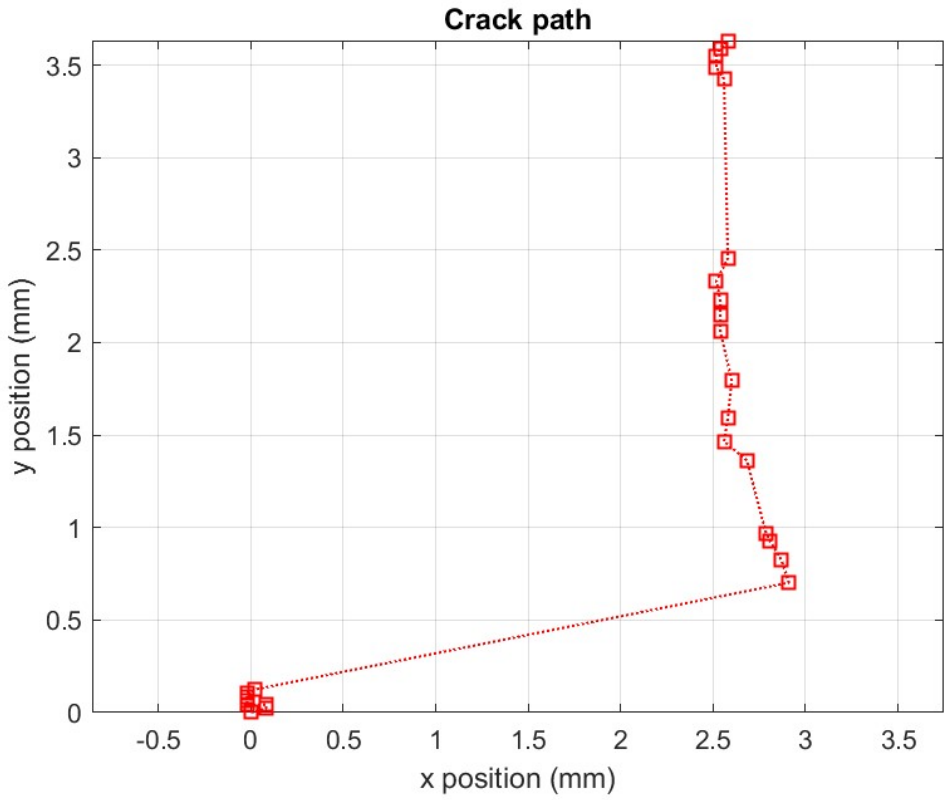

Figure 5.9 Crack path for L3-4X-S1e4.

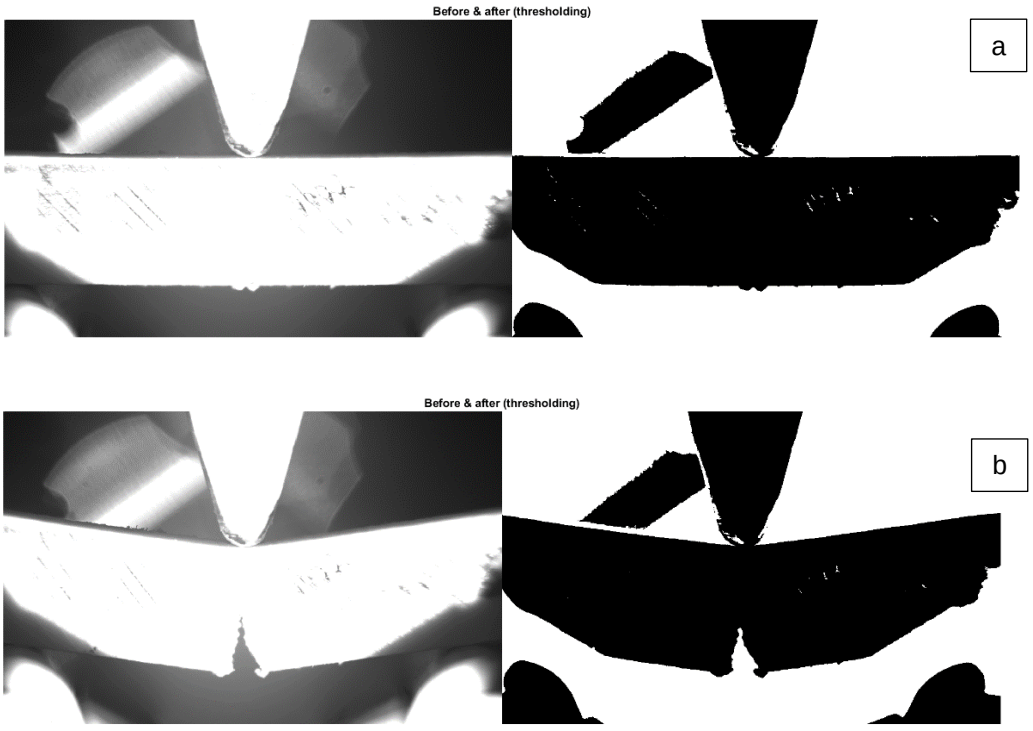

Figure 5.10 L3-4X-S1e4: (a) start frame and (b) end frame.

This behavior was expected since the material was uniform in the y-axis. Looking at the crack propagation in time, all E samples had a slow and steady crack progression with an occasional burst where the crack spiked in speed. Since E samples were uniform in the y-axis, it was more interesting to look at the first burst of crack speed instead of the whole curve because the evolution was mostly related to the sample's structural integrity [3] and does not tell much about the effects of the pattern. The script did not use an infinite number of points for its graphs so the time *t* at which the first burst appeared was roughly estimated as the first point before a visual spike (example in Figure 5.11).

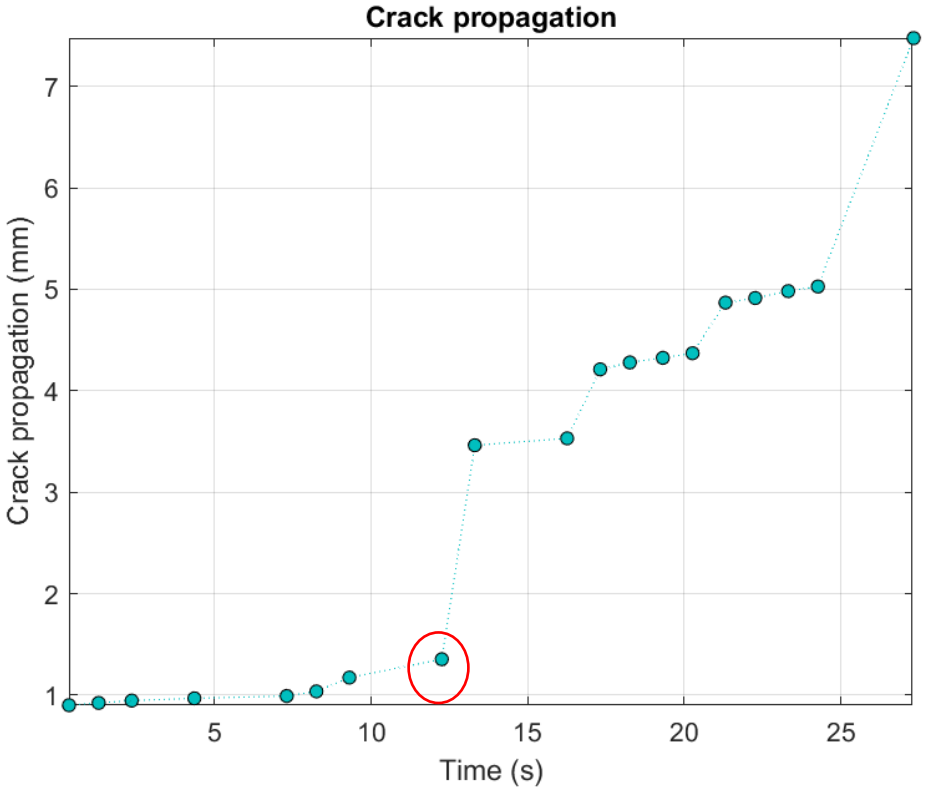

Figure 5.11 Crack propagation of L0e5 (start of crack burst is circled in red).

Figure 5.12 shows the time at which the first big burst appeared disrupting the linear progression of the crack. It was observed that L0 and S patterns tended to experience the burst earlier compared to the other patterns that could be analyzed. An average for first burst apparition was at 14.9 sec and 13.0 sec, respectively. On the contrary, L3-4X-S1 with the most peened layers seemed to slow down the apparition of burst significantly with an average of 21.5 sec. L3-3X-S4 and L1-3X-S7, both with three peened layers, also showed good performance when delaying the burst with an average of 19.4 sec and 18.7 sec, respectively. These results seem to indicate that in a solicitation parallel to the induced CRS direction, the parameter that matters was the number of peened layers more than their position in the sample. This could be contradicted by the results of L0 and S; however, looking at the standard deviation of those results, it can be conjectured that the small amount of peening present in the S samples did not provide a significant difference from the unpeened samples.

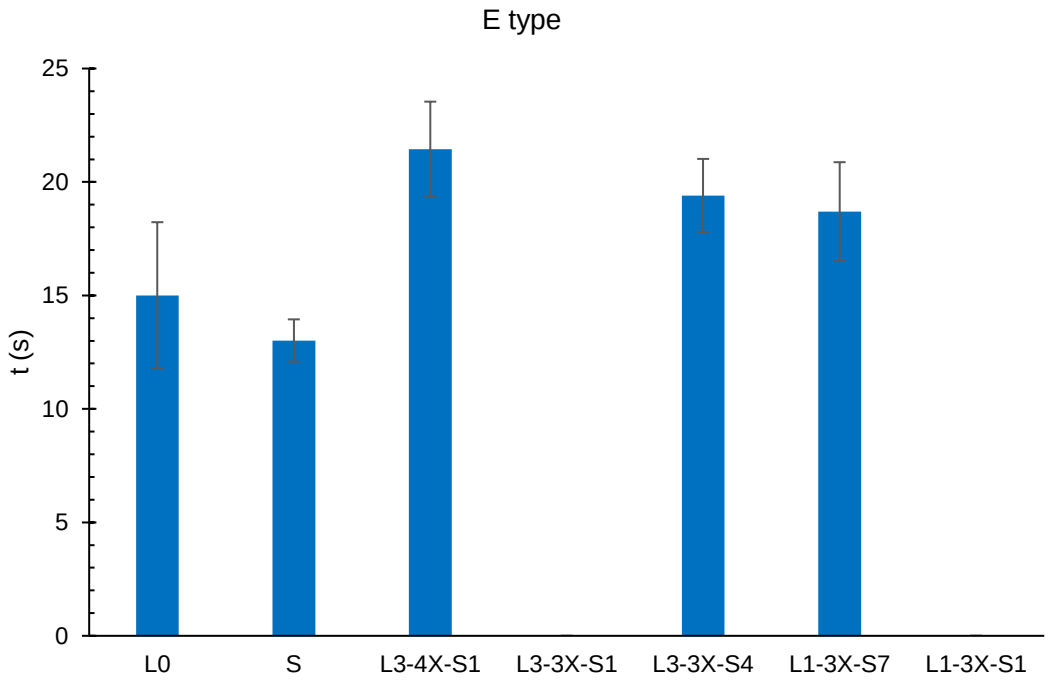

Figure 5.12 Time of apparition of the first burst of crack.

F Type samples

F type samples have very different crack curves compared to E type samples. Typically, the crack path curves have heavy variations along the y-axis as shown in Figure 5.13. It is conjectured that these variations correspond to the crack hitting a new layer after coming through the previous one. The crack then followed the new layer before finding a new weak spot to continue propagating. A good visual indicator of this phenomenon can be found when zooming in on the cracks of some samples like in L1-3X-S1f samples, where the jagged edges of the crack corresponding to different layers of the sample were clearly observed (Figure 5.14).

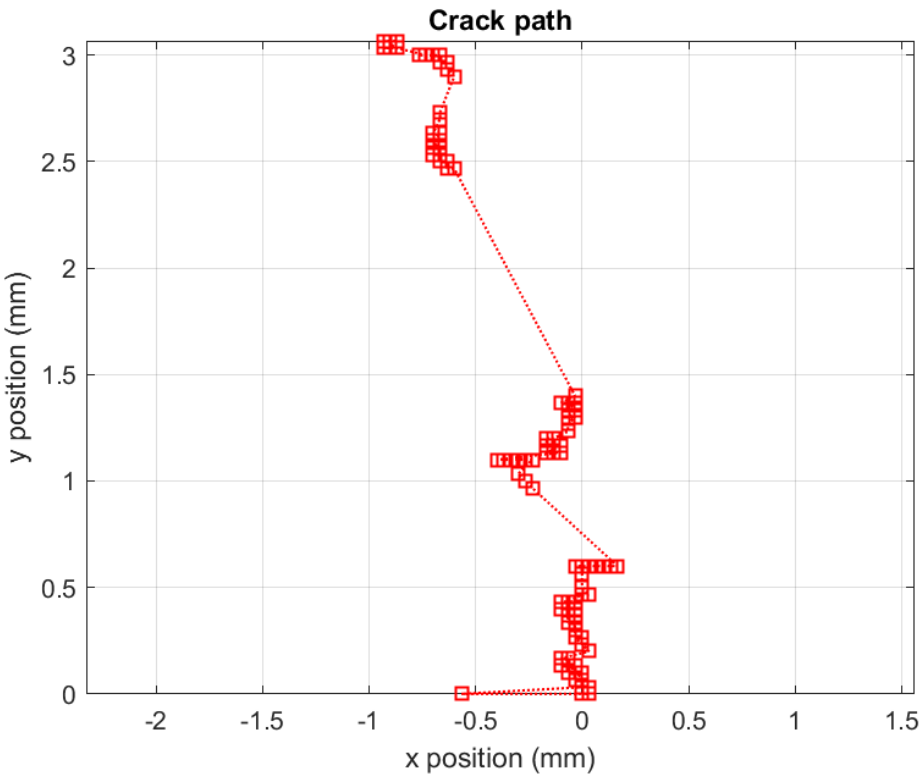

Figure 5.13 Heavy variation of crack path along the x-axis (L1-3X-S1f1).

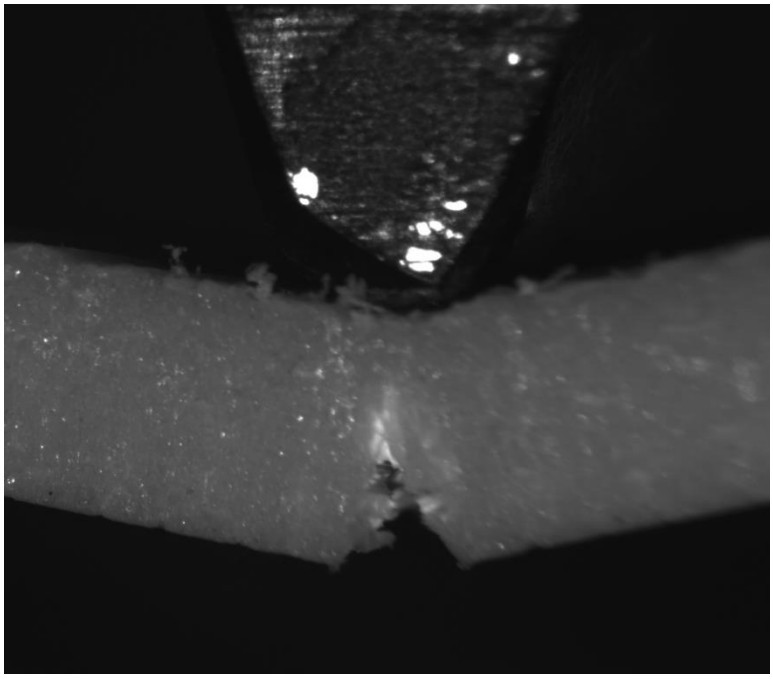

Figure 5.14 Crack with jagged edges corresponding to the internal layers of the material.

In the same idea, when analyzing the curves of crack propagation over time, all the analyzed samples can be classified into three categories: bottom stack, top stack, and combined mode. Samples that have their bottom layers peened with spread out treated layers, like the L1-3X-S7f and L3-4x-S1 patterns, had cracks that stop on few to no layers (typically 1 or 2). This wass represented by a long plateau in the crack propagation graph with big burst of the crack between stops. These samples typically had a relatively short initial plateau, meaning the first burst happens quite soon in the deformation of the sample. The first burst was 26.3 sec on average for L1-3X-S7f type and 27.9 sec on average for L3-4x-S1f type. Since all the peening was stacked at the bottom, once the crack grew past those layers, it rapidly propagates through the other "softer" homogeneous layers. Figure 5.15 illustrates a typical crack propagation curve for this type of sample.

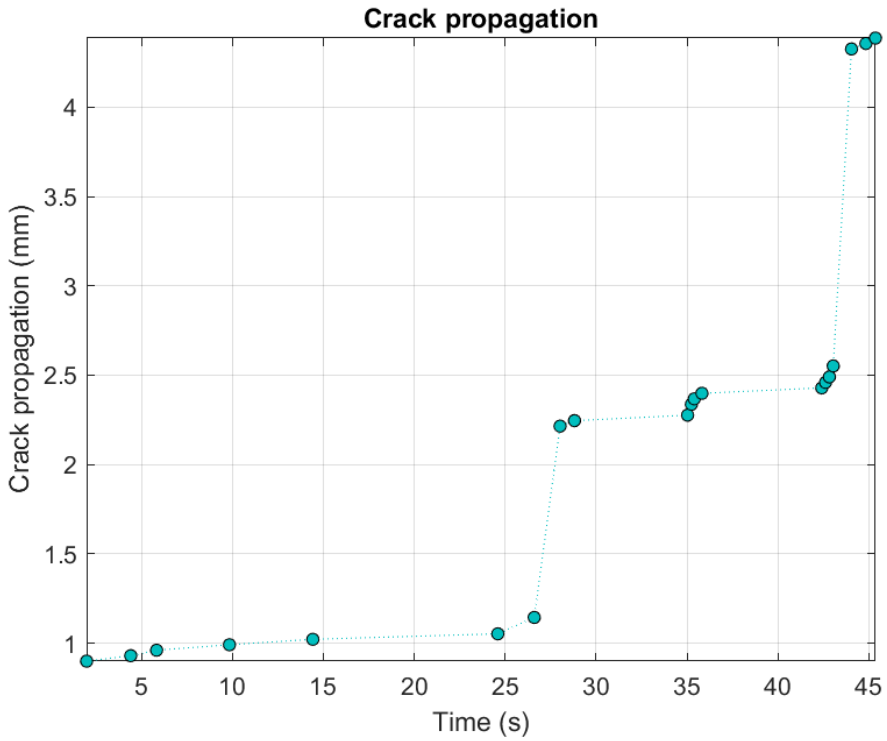

Figure 5.15 Crack propagation of L3-4X-S1f2.

Samples that have their peening stacked at the top, meaning the L3-3X-S1 and L1-3X-S1 patterns, tended to have a very slow opening, meaning either very long initial plateau or a very steady propagation with a very small slope. Some samples experience very small burst but nothing comparable to the number and intensity of the first category. However, these samples tended to experience a very intense burst at the end of the plateau that usually made up most of the crack's length. This burst happened on average at 43.2 sec for L1-3X-S1f and 42.6 sec. This behavior could be related to the peened layers but could also be due to a higher cohesion between non-peened layers that are at the bottom. Not having an alternation of peened and unpeened layers must reduce the chances of having interfacial effects between layers. Figure 5.16 illustrates a typical crack propagation curve for this type of samples.

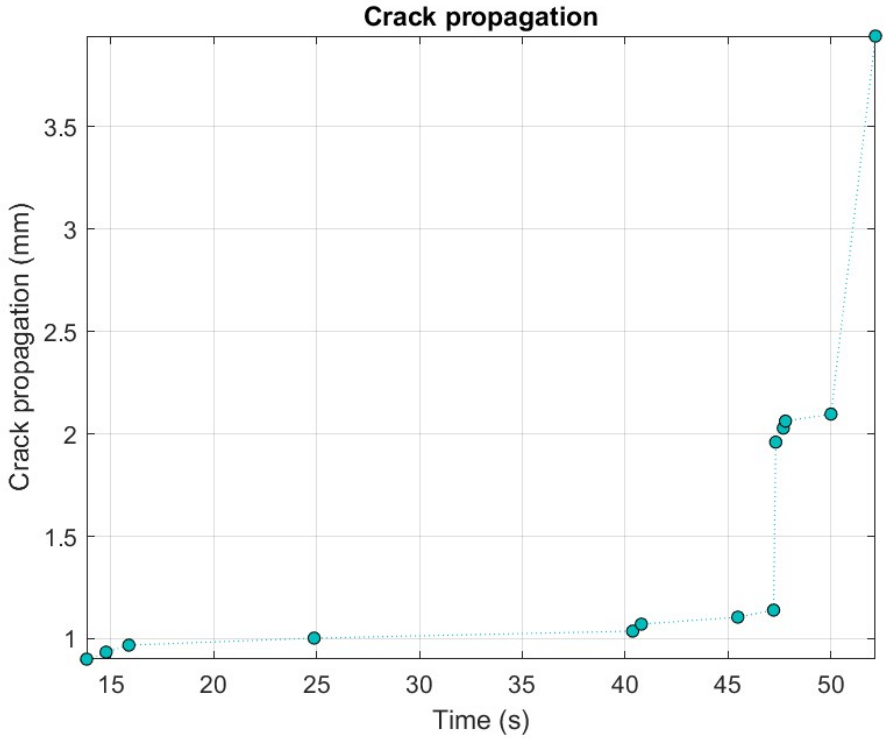

Figure 5.16 Crack propagation of L3-3X-S1f2.

L3-3X-S4f type samples seem to be a combination of the previously described categories with a lot more plateaus (typically 3 or 4) and shorter bursts in between. The apparition of the first burst was also delayed compared to the first category while appearing faster than the top peened samples with an average of 33.9 sec. This seems odd since L3-3X-S4 was also a bottom peened sample. However, L3-3X-S4 did have the higher stiffness post impact when tested by DMA in Chapter 3. This could correlate to better structural integrity [3] that allowed it to exploit its peened layers better than L3-4X-S1 that was very similar in treatment repartition. Figure 5.17 illustrates a typical crack propagation curve for this type of samples.

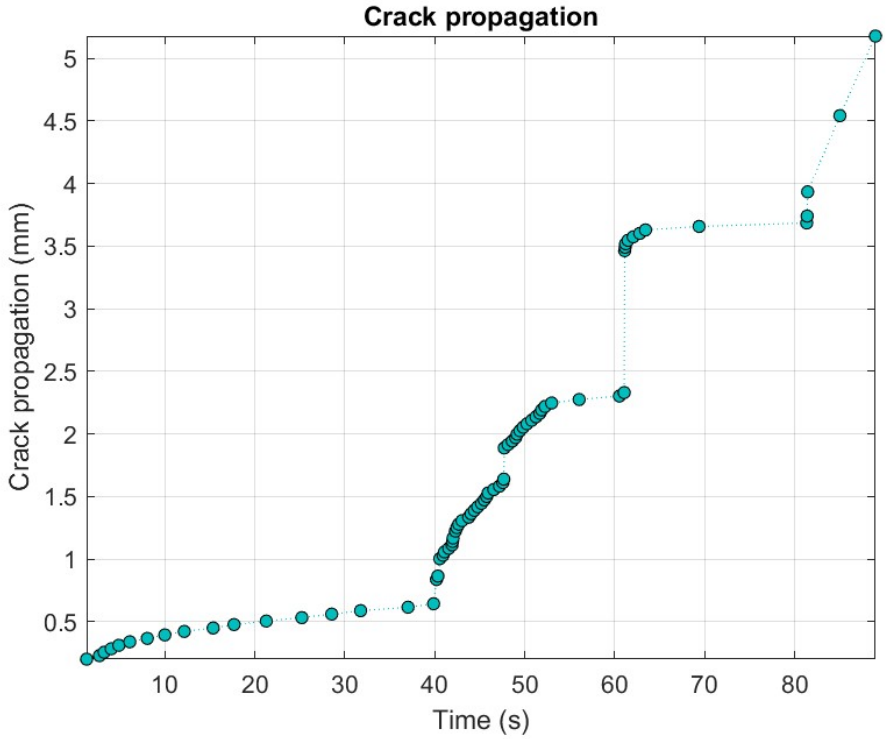

Figure 5.17 Crack propagation of L3-3X-S4f1.

5.4 Summary and Conclusions

This experiment completes the drop test results described in Chapter 3. In a slower perspective, it was possible to have a more nuanced view of the effect of LSP on a multilayer material. It is important to keep in mind that these samples were cut from already fragilized material so not everything can be compared directly to the results of the drop test. However, some similarities were still noticeable. For instance, L3-4X-S1 type samples still stood out regarding stiffness related performance. This pattern, on average, provided a better resistance to deformation with the highest applied load to achieve average maximum deformation compared to the other patterns. Poor results in terms of resistance to deformation in the edge position once again highlighted the delamination related issues encountered with L3-3X-S1 type samples. However, delamination did not seem to hinder the resistance to crack propagation of L3-3X-S1

samples in the flat position since they showed one of the longest resistances to first burst out of all the samples. This seems to correlate well with the fact that L3-3X-S1 samples were found to be the most elastic of all samples when looking at the load-displacement curves. It is possible that decreasing the layer-to-layer cohesion allowed for better elasticity since single layers were more malleable than the final print.

Regarding the resistance to crack propagation parallel to the CRSs (E orientation), it seemed that having the greatest number of layers was the better solution since the longest average delay of the first crack burst came from L3-4X-S1e samples and the worst samples in that regard were L0e and Se types. More nuanced results can be found when looking at resistance to crack propagation perpendicular to the CRSs (F orientation). In this case, it seems that having top stacked LSP treatment can more efficiently delay the apparition of the first burst like the results from L3-3X-S1f and L1-3X-S1f demonstrated. However, having peening stacked at the bottom of the sample seemed to provide a more gradual failure of the samples with more plateaus and shorter bursts. L3-3X-S4 seemed to be the most efficient pattern in that regard but it could be due to a better structural integrity post impact resistance test. Whether these results were a purely caused by LSP or due to interfacial effects between layers based on if they were peened or not needs to be investigated. If L0 samples could have been properly analyzed, it might haven given some indications on which is the correct theory.

CHAPTER 6

SUMMARY AND CONCLUSIONS

6.1 Summary

The thermo-mechanical effects of LSP applied to a multi-layered polymer material and the feasibility of the hybrid AM process itself were investigated in this study. The knowledge gained from this research can be summarized in the following statements:

- LSP on polymers seemed to be a promising manufacturing technique and could help to modify multiple mechanical properties of a material. One of the main characteristics of LSP is variation of stiffness and resistance to deformation after treatment on PLA.
- The variation of stiffness relative to where LSP was applied in a multilayer material depended on the peening pattern.
- Higher number of evenly spread peened layers seemed to improve the durability of the material during an impact scenario.
- Accumulation of peened layers on the side facing away from the impact seemed to decrease the durability of the material during an impact scenario.
- The hybrid AM process used in this study decreased the layer-to-layer cohesion of the material.
- Presence of LSP treatment slightly influences the material's relaxation, but the impact of treatment distribution or quantity is not clearly highlighted with the applied treatment density.

- In the case of small amplitude thermo-mechanical solicitation, the presence of LSP can increase the stiffness of the material, but the potential growth in stiffness seems to rapidly cap out and peening more than two layers does not seem greatly beneficial.
- In the case of small amplitude thermo-mechanical solicitation, repartition of treatment in the material did not seem to significantly increase stiffness.
- Having a higher number of peened layers seemed to be more efficient for deformation resistance in the case of a solicitation perpendicular to the treated layers.
- Stacking LSP treatment at the top of the sample was also confirmed to be more efficient for bending resistance compared to bottom stacking the treatment in the case of slow deformation.
- Top stacking the treatment delayed the burst in crack propagation for a slow deformation, but bottom stacking seems to provide more chances to stop the crack after the first burst especially when spreading out the layers.

6.2 Conclusions

The alteration of stiffness values, impact energy absorption, and resistance to slow deformation properties of the material demonstrates that LSP can be used to modify a polymer's mechanical properties. The behavior of the samples with different peening patterns also proved that repartition of the surface treatment is important in a multilayered material. It was conjectured that the induced compressive residual stress from LSP would increase the stiffness of the treated layer. Therefore, it was expected that stacking the treatment on the side facing away from an impact would give the samples better durability since the higher stiffness would help dissipate the high stress

generated on the bottom the side of the sample during the impact. However, it was observed that this theory was wrong and bottom stacking the treatment made the material less durable both in impact resistance and bending resistance. It is hypothesized that LSP did increase the stiffness of individual layers looking at the results from non-bottom-stacked samples, but the compressive residual stresses added to the high stress generated during the impact made the bottom layers reach their elastic limit faster. Distributing the LSP treatment evenly throughout the material seems to be the most efficient way of increasing the overall stiffness while gaining some durability.

With the results of the DMA test, a much more noticeable stiffness increase was observed for peened samples. However, the difference in stiffness when increasing the number of peened layers was not very important compared to the difference between non-peened and peened samples. This observation implies that in the case of small amplitude thermo-mechanical solicitation, it is possible to maximize the improvement in mechanical properties with only a small amount of LSP. No influence on the other tested properties was clearly observed and no assumption could be made on whether spreading or stacking LSP was beneficial for the tested properties.

An important observation was that the stiffness increase was not observed on a similar scale and for similar samples in the drop test and DMA. In some experiments, applying LSP smartly was more important than just having more peened layers. The better performing samples were also different depending on the investigated properties and used method. It is true that some samples stood out in multiple test phase, such as L3-4x-S1; however, the superiority of this pattern was not always proven with other patterns performing better in areas where L3-4x-S1 was on the weaker side. This implies that there is no superior distribution of treatment or amount of treatment applied. The right solution will depend on what properties one is trying to improve and

for what type of solicitation. This is a promising conclusion for the future as it demonstrates that increasing the amount of treatment and having a regular or non-regular spread will not always be the best choice. Every option could be viable depending on the expected result.

6.3 Future Work

A lot of difficulties in this work came from the fact that peening density was too low leading to a lot of uncertainties and potentially reduced effects on the different tests that were performed. For future work, a more practical and automated way of applying interlayer LSP needs to be developed as well as focusing on smaller peening surfaces to minimize the amount of time and resources needed to prepare samples. More specialized tests in combination with higher density of peening might reveal some more noticeable impacts on relaxation phenomenon or rejuvenation due to the induced stress. The stiffness of a material can be influenced by the hybrid AM method described in this study. However, the exact effect of LSP treatment on this parameter needs to be investigated in order to understand how the density of treatment and distribution within the material can be used to control the variation of stiffness. The delamination issue also needs further looking into to see if high amount of LSP might start damaging the sample or influence the layer cohesion. The actual amount of induced compressive residual stress by one laser shot based on power and area also needs to be investigated to make the research of the potential effects on the material properties easier.

REFERENCES

1. Chapter 1

[1] S.H. Ghaffar, J. Corker, M. Fan, Additive manufacturing technology and its implementation in construction as an eco-innovative solution, Autom. Constr. 93 (2018) 1–11. https://doi.org/10.1016/j.autcon.2018.05.005.

[2] M.E. Korkmaz, S. Waqar, A. Garcia-Collado, M.K. Gupta, G.M. Krolczyk, A technical overview of metallic parts in hybrid additive manufacturing industry, J. Mater. Res. Technol. 18 (2022) 384–395. https://doi.org/10.1016/j.jmrt.2022.02.085.

[3] A. Al Rashid, S.A. Khan, S. G. Al-Ghamdi, M. Koç, Additive manufacturing: Technology, applications, markets, and opportunities for the built environment, Autom. Constr. 118 (2020) 103268. https://doi.org/10.1016/j.autcon.2020.103268.

[4] A. Al Rashid, S.A. Khan, S. G. Al-Ghamdi, M. Koç, Additive manufacturing of polymer nanocomposites: Needs and challenges in materials, processes, and applications, J. Mater. Res. Technol. 14 (2021) 910–941. https://doi.org/10.1016/j.jmrt.2021.07.016.

[5] H. Monteiro, G. Carmona-Aparicio, I. Lei, M. Despeisse, Energy and material efficiency strategies enabled by metal additive manufacturing – A review for the aeronautic and aerospace sectors, Energy Rep. 8 (2022) 298–305. https://doi.org/10.1016/j.egyr.2022.01.035.

[6] S. Ford, M. Despeisse, Additive manufacturing and sustainability: an exploratory study of the advantages and challenges, J. Clean. Prod. 137 (2016) 1573–1587. https://doi.org/10.1016/j.jclepro.2016.04.150.

[7] L. Agnusdei, A. Del Prete, Additive manufacturing for sustainability: A systematic literature review, Sustain. Futur. 4 (2022) 100098. https://doi.org/10.1016/j.sftr.2022.100098.

[8] A. Al-khazraji, A. A. Mutasher, Effect of Laser Shock Peening on the Fatigue Behavior and Mechanical Properties of Composite Materials, Al-Khwarizmi Eng. J. 15 (2019) 1–9. https://doi.org/10.22153/kej.2019.08.004.

[9] R.A. Buswell, W.R. Leal de Silva, S.Z. Jones, J. Dirrenberger, 3D printing using concrete extrusion: A roadmap for research, Cem. Concr. Res. 112 (2018) 37–49. https://doi.org/10.1016/j.cemconres.2018.05.006.

[10] E. Maleki, S. Bagherifard, M. Bandini, M. Guagliano, Surface post-treatments for metal additive manufacturing: Progress, challenges, and opportunities, Addit. Manuf. 37 (2021) 101619. https://doi.org/10.1016/j.addma.2020.101619.

[11] S.K. Nemani, R.K. Annavarapu, B. Mohammadian, A. Raiyan, J. Heil, Md.A. Haque, A. Abdelaal, H. Sojoudi, Surface Modification of Polymers: Methods and Applications, Adv. Mater. Interfaces. 5 (2018) 1801247. https://doi.org/10.1002/admi.201801247.

[12] X. Tian, T. Liu, C. Yang, Q. Wang, D. Li, Interface and performance of 3D printed continuous carbon fiber reinforced PLA composites, Compos. Part Appl. Sci. Manuf. 88 (2016) 198–205. https://doi.org/10.1016/j.compositesa.2016.05.032.

[13] A. Siddika, Md.A.A. Mamun, W. Ferdous, A.K. Saha, R. Alyousef, 3D-printed concrete: applications, performance, and challenges, J. Sustain. Cem.-Based Mater. 9 (2020) 127–164. https://doi.org/10.1080/21650373.2019.1705199.

[14] R. Govender, E.O. Kissi, A. Larsson, I. Tho, Polymers in pharmaceutical additive manufacturing: A balancing act between printability and product performance, Adv. Drug Deliv. Rev. 177 (2021) 113923. https://doi.org/10.1016/j.addr.2021.113923.

[15] I. Gibson, D. Rosen, B. Stucker, Additive Manufacturing Technologies: 3D Printing, Rapid Prototyping, and Direct Digital Manufacturing, Springer, New York, NY, 2015. https://doi.org/10.1007/978-1-4939-2113-3.

[16] Contour Crafting Corporation | Construction 3D Printing | California, CC Corp. (n.d.). https://www.contourcrafting.com (accessed November 7, 2023).

[17] F. Regina, F. Lavecchia, L.M. Galantucci, Preliminary study for a full colour low cost open source 3D printer, based on the combination of fused deposition modelling (FDM) or fused filament fabrication (FFF) and inkjet printing, Int. J. Interact. Des. Manuf. IJIDeM. 12 (2018) 979–993. https://doi.org/10.1007/s12008-017-0432-x.

[18] FDM vs. FFF: Differences and Comparison, (n.d.). https://www.xometry.com/resources/3d-printing/fdm-vs-fff-3d-printing/ (accessed November 7, 2023).

[19] Z. Weng, J. Wang, T. Senthil, L. Wu, Mechanical and thermal properties of ABS/montmorillonite nanocomposites for fused deposition modeling 3D printing, Mater. Des. 102 (2016) 276–283. https://doi.org/10.1016/j.matdes.2016.04.045.

[20] N. Shahrubudin, T.C. Lee, R. Ramlan, An Overview on 3D Printing Technology: Technological, Materials, and Applications, Procedia Manuf. 35 (2019) 1286–1296. https://doi.org/10.1016/j.promfg.2019.06.089.

[21] J.Z. Zhou, S. Huang, L.D. Zuo, X.K. Meng, J. Sheng, Q. Tian, Y.H. Han, W.L. Zhu, Effects of laser peening on residual stresses and fatigue crack growth properties of Ti–6Al–4V titanium alloy, Opt. Lasers Eng. 52 (2014) 189–194. https://doi.org/10.1016/j.optlaseng.2013.06.011.

[22] Y. Sano, K. Akita, T. Sano, A Mechanism for Inducing Compressive Residual Stresses on a Surface by Laser Peening without Coating, Metals. 10 (2020) 816. https://doi.org/10.3390/met10060816.

[23] C. Zhang, Y. Dong, C. Ye, Recent Developments and Novel Applications of Laser Shock Peening: A Review, Adv. Eng. Mater. 23 (2021) 2001216. https://doi.org/10.1002/adem.202001216.

[24] C.S. Montross, T. Wei, L. Ye, G. Clark, Y.-W. Mai, Laser shock processing and its effects on microstructure and properties of metal alloys: a review, Int. J. Fatigue. 24 (2002) 1021–1036. https://doi.org/10.1016/S0142-1123(02)00022-1.

[25] N. Kalentics, E. Boillat, P. Peyre, S. Ćirić-Kostić, N. Bogojević, R.E. Logé, Tailoring residual stress profile of Selective Laser Melted parts by Laser Shock Peening, Addit. Manuf. 16 (2017) 90–97. https://doi.org/10.1016/j.addma.2017.05.008.

[26] M.P. Sealy, H. Hadidi, L.D. Sotelo, W.L. Li, J.A. Turner, J.A. McGeough, Compressive behavior of 420 stainless steel after asynchronous laser processing, CIRP Ann. 69 (2020) 169–172. https://doi.org/10.1016/j.cirp.2020.04.059.

[27] H. Hadidi, B. Mailand, T. Sundermann, E. Johnson, G. Madireddy, M. Negahban, L. Delbreilh, M. Sealy, Low velocity impact of ABS after shot peening predefined layers during additive manufacturing, Procedia Manuf. 34 (2019) 594–602. https://doi.org/10.1016/j.promfg.2019.06.169.

[28] H. Hadidi, B. Mailand, T. Sundermann, E. Johnson, R. Karunakaran, M. Negahban, L. Delbreilh, M. Sealy, Dynamic Mechanical Analysis of ABS From Hybrid Additive Manufacturing by Fused Filament Fabrication and Shot Peening, in: American Society of Mechanical Engineers Digital Collection, 2021. https://doi.org/10.1115/MSEC2020-8253.

[29] Polymer Market Size, Share & Growth Forecast Report 2030, PS Intell. (2023). https://www.psmarketresearch.com/market-analysis/polymer-market (accessed June 8, 2023).

[30] S. Saleh Alghamdi, S. John, N. Roy Choudhury, N.K. Dutta, Additive Manufacturing of Polymer Materials: Progress, Promise and Challenges, Polymers. 13 (2021) 753. https://doi.org/10.3390/polym13050753.

[31] J. Brady, T. Dürig, P.I. Lee, J.-X. Li, Chapter 7 - Polymer Properties and Characterization, in: Y. Qiu, Y. Chen, G.G.Z. Zhang, L. Yu, R.V. Mantri (Eds.), Dev. Solid Oral Dos. Forms Second Ed., Academic Press, Boston, 2017: pp. 181–223. https://doi.org/10.1016/B978-0-12-802447-8.00007-8.

[32] G. Ying, N. Jiang, C. Yu, Y.S. Zhang, Three-dimensional bioprinting of gelatin methacryloyl (GelMA), Bio-Des. Manuf. 1 (2018) 215–224. https://doi.org/10.1007/s42242-018-0028-8.

[33] A. Basu, A. Saha, C. Goodman, R.T. Shafranek, A. Nelson, Catalytically Initiated Gel-in-Gel Printing of Composite Hydrogels, ACS Appl. Mater. Interfaces. 9 (2017) 40898–40904. https://doi.org/10.1021/acsami.7b14177.

[34] Ö. Özbek, Ö.Y. Bozkurt, A. Erkliğ, LOW VELOCITY IMPACT BEHAVIORS OF BASALT/EPOXY REINFORCED COMPOSITE LAMINATES WITH DIFFERENT FIBER ORIENTATIONS, Turk. J. Eng. 4 (2020) 197–202. https://doi.org/10.31127/tuje.644025.

[35] J.R.C. Dizon, A.H. Espera, Q. Chen, R.C. Advincula, Mechanical characterization of 3D-printed polymers, Addit. Manuf. 20 (2018) 44–67. https://doi.org/10.1016/j.addma.2017.12.002.

[36] M. Mehrabi Mazidi, A. Edalat, R. Berahman, F.S. Hosseini, Highly-Toughened Polylactide- (PLA-) Based Ternary Blends with Significantly Enhanced Glass Transition and Melt Strength: Tailoring the Interfacial Interactions, Phase Morphology, and Performance, Macromolecules. 51 (2018) 4298–4314. https://doi.org/10.1021/acs.macromol.8b00557.

[37] N.S. Murthy, X-ray Diffraction from Polymers, in: Polym. Morphol., John Wiley & Sons, Ltd, 2016: pp. 14–36. https://doi.org/10.1002/9781118892756.ch2.

[38] S. Zhang, T.R. Hull, A.R. Horrocks, G. Smart, B.K. Kandola, J. Ebdon, P. Joseph, B. Hunt, Thermal degradation analysis and XRD characterisation of fibre-forming synthetic polypropylene containing nanoclay, Polym. Degrad. Stab. 92 (2007) 727–732. https://doi.org/10.1016/j.polymdegradstab.2006.12.001.

[39] UV degradation of clay-reinforced polypropylene nanocomposites - Ben Hadj Salah - 2016 - Polymer Engineering & Science - Wiley Online Library, (n.d.). https://4spepublications.onlinelibrary.wiley.com/doi/abs/10.1002/pen.24273 (accessed November 12, 2023).

[40] J.H. Butler, D.C. Joy, G.F. Bradley, S.J. Krause, Low-voltage scanning electron microscopy of polymers, Polymer. 36 (1995) 1781–1790. https://doi.org/10.1016/0032-3861(95)90924-Q.

[41] D. Campbell, R.A. Pethrick, J.R. White, Polymer Characterization: Physical Techniques, 2nd Edition, CRC Press, 2017.

[42] A.L. Pereira, M.D. Banea, J.S.S. Neto, D.K.K. Cavalcanti, Mechanical and Thermal Characterization of Natural Intralaminar Hybrid Composites Based on Sisal, Polymers. 12 (2020) 866. https://doi.org/10.3390/polym12040866.

2. Chapter 2

[1] Standard Test Method for Measuring the Damage Resistance of a Fiber-Reinforced Polymer Matrix Composite to a Drop-Weight Impact Event, (n.d.). https://www.astm.org/d7136_d7136m-15.html (accessed November 8, 2023).

[2] C. Le Bras, A. Rondepierre, R. Seddik, M. Scius-Bertrand, Y. Rouchausse, L. Videau, B. Fayolle, M. Gervais, L. Morin, S. Valadon, R. Ecault, D. Furfari, L. Berthe, Laser Shock Peening: Toward the Use of Pliable Solid Polymers for Confinement, Metals. 9 (2019) 793. https://doi.org/10.3390/met9070793.

[3] E. Maleki, S. Bagherifard, M. Bandini, M. Guagliano, Surface post-treatments for metal additive manufacturing: Progress, challenges, and opportunities, Addit. Manuf. 37 (2021) 101619. https://doi.org/10.1016/j.addma.2020.101619.

[4] G. Klein, Experimental Investigation on Thermally Induced Residual Stress Redistribution from Interlayer Laser Shock Peening During Additive Manufacturing, Embargoed Masters Theses. (2022). https://digitalcommons.unl.edu/embargotheses/236.

3. Chapter 3

[1] H. Hadidi, B. Mailand, T. Sundermann, E. Johnson, G. Madireddy, M. Negahban, L. Delbreilh, M. Sealy, Low velocity impact of ABS after shot peening predefined layers during additive manufacturing, Procedia Manuf. 34 (2019) 594–602. https://doi.org/10.1016/j.promfg.2019.06.169.

[2] A. Zemanová, J. Zeman, M. Šejnoha, Simple Numerical Model of Laminated Glass Beams, Acta Polytech. 48 (2008). https://doi.org/10.14311/1065.

[3] B. Liu, L.B. Lessard, Fatique and damage-tolerance analysis of composite laminates: Stiffness loss, damage-modelling, and life prediction, Compos. Sci. Technol. 51 (1994) 43–51. https://doi.org/10.1016/0266-3538(94)90155-4.

4. Chapter 4

[1] L. Santonja-Blasco, R. Moriana, J.D. Badía, A. Ribes-Greus, Thermal analysis applied to the characterization of degradation in soil of polylactide: I. Calorimetric and viscoelastic analyses, Polym. Degrad. Stab. 95 (2010) 2185–2191. https://doi.org/10.1016/j.polymdegradstab.2010.08.005.

[2] F.X. Espinach, S. Boufi, M. Delgado-Aguilar, F. Julián, P. Mutjé, J.A. Méndez, Composites from poly(lactic acid) and bleached chemical fibres: Thermal properties, Compos. Part B Eng. 134 (2018) 169–176. https://doi.org/10.1016/j.compositesb.2017.09.055.

[3] R. Esmaeeli, H. Aliniagerdroudbari, S.R. Hashemi, C. Jbr, S. Farhad, Designing a New Dynamic Mechanical Analysis (DMA) System for Testing Viscoelastic Materials at High Frequencies, Model. Simul. Eng. 2019 (2019) e7026267. https://doi.org/10.1155/2019/7026267.

[4] PolyLite™ PLA, Polymaker. (2023). https://polymaker.com/product/polylite-pla/ (accessed November 7, 2023).

[5] M. Cristea, D. Ionita, M.M. Iftime, Dynamic Mechanical Analysis Investigations of PLA-Based Renewable Materials: How Are They Useful?, Materials. 13 (2020) 5302. https://doi.org/10.3390/ma13225302.

[6] C. Bauwens-Crowet, J.-C. Bauwens, Effect of annealing on the shear yield stress of rejuvenated polycarbonate, Polymer. 29 (1988) 1985–1989. https://doi.org/10.1016/0032-3861(88)90171-1.

[7] M. Mehrabi Mazidi, A. Edalat, R. Berahman, F.S. Hosseini, Highly-Toughened Polylactide- (PLA-) Based Ternary Blends with Significantly Enhanced Glass Transition and Melt Strength: Tailoring the Interfacial Interactions, Phase Morphology, and Performance, Macromolecules. 51 (2018) 4298–4314. https://doi.org/10.1021/acs.macromol.8b00557.

5. Chapter 5

[1] Standard Test Method for Measurement of Fracture Toughness, (n.d.). https://www.astm.org/e1820-21.html (accessed November 24, 2023).

[2] B. Vieille, C. Keller, M. Mokhtari, H. Briatta, T. Breteau, J. Nguejio, F. Barbe, M. Ben Azzouna, E. Baustert, Investigations on the fracture behavior of Inconel 718 superalloys obtained from cast and additive manufacturing processes, Mater. Sci. Eng. A. 790 (2020) 139666. https://doi.org/10.1016/j.msea.2020.139666.

[3] G.C. Sih, Multiscale Fatigue Crack Initiation and Propagation of Engineering Materials: Structural Integrity and Microstructural Worthiness: Fatigue Crack Growth Behaviour of Small and Large Bodies, Springer Science & Business Media, 2008.

APPENDIX

1. Impact plate geometry

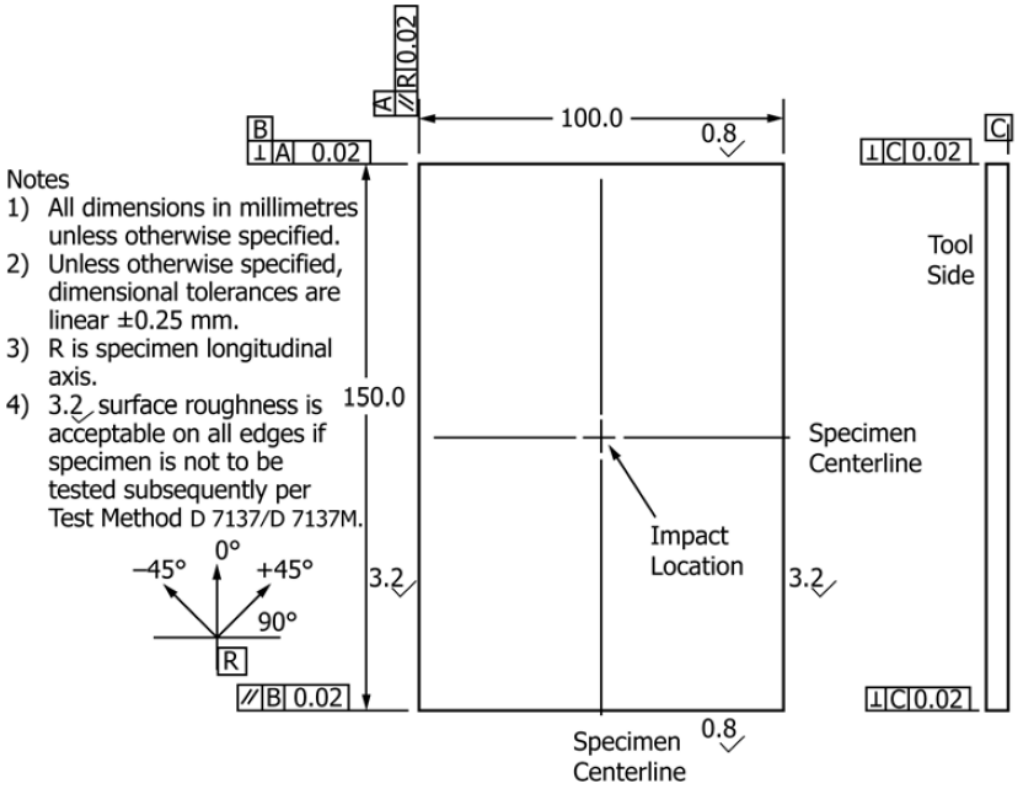

2. Printing default, layer starting in the middle of previous layer

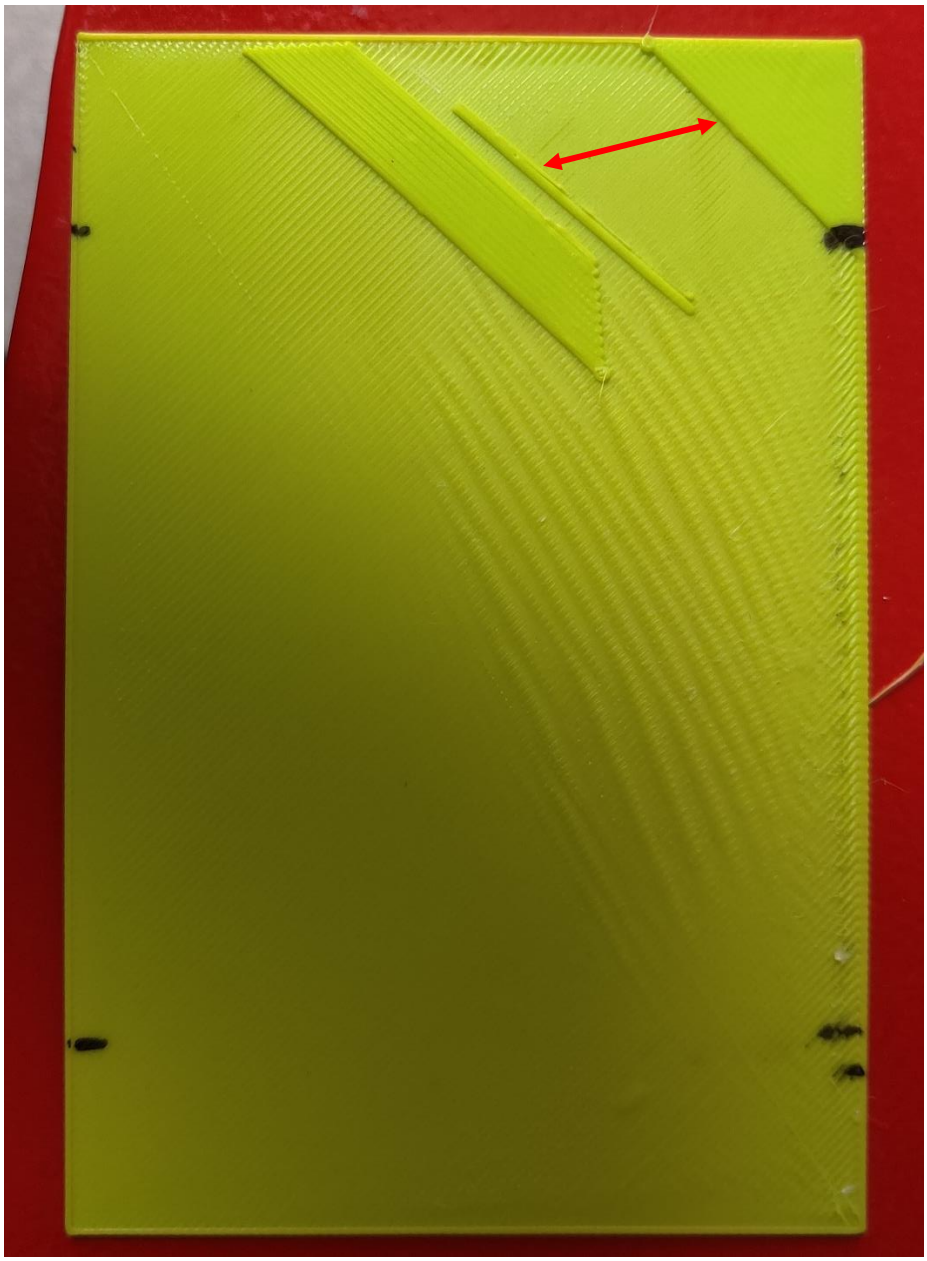

3. Using weights to maintain adhesion of the sample after printbed removal

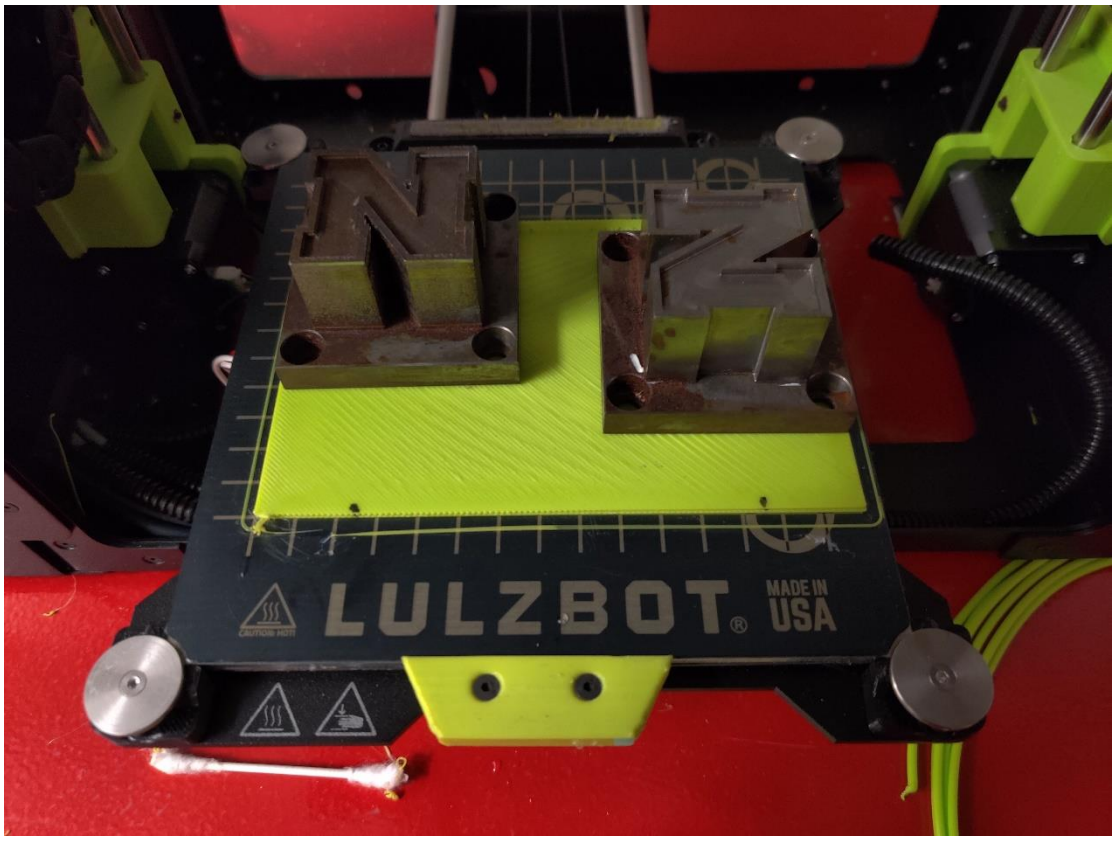

4. Printing default

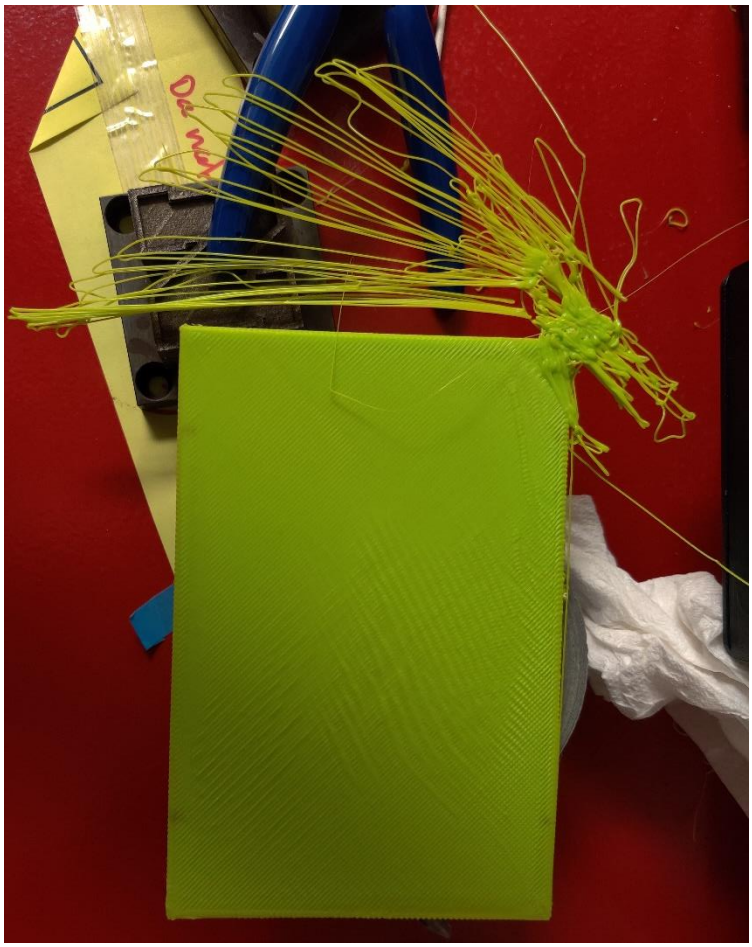

5. Beam assumption and equations

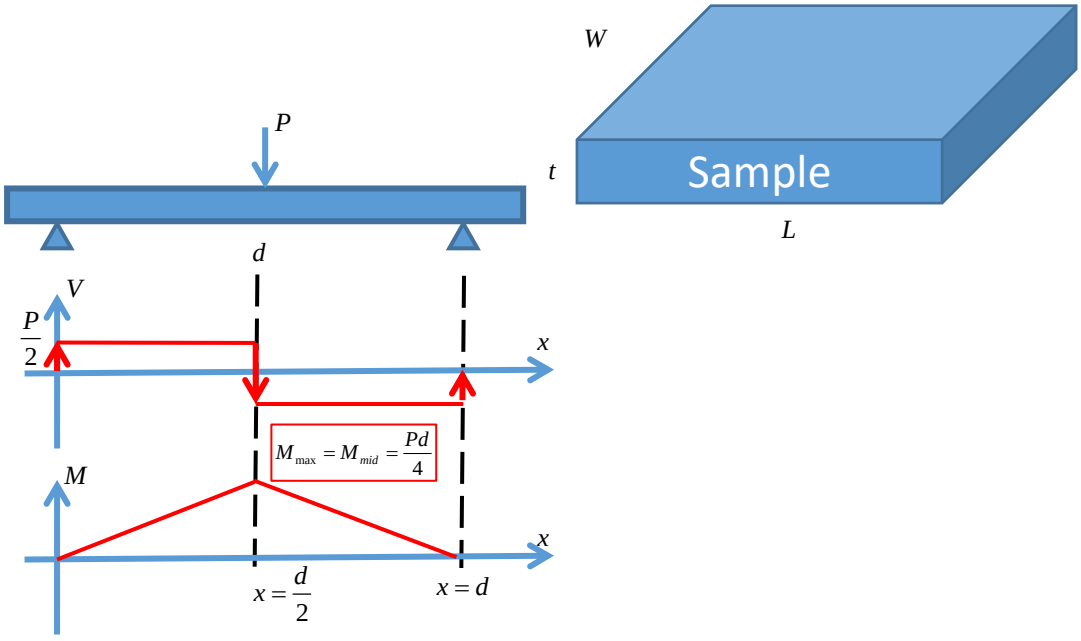

Mechanics of materials: Beam assumption

Curvature: κ

Strain: $\varepsilon = -\kappa y$

Stress: $\sigma = E(y)\varepsilon = -E(y)\kappa y$

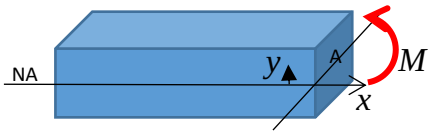

Moment: $M = -\int_A \sigma y dA = \kappa \int_A E(y) y^2 dA$

Effective bending: $k_B = \overline{EI} \equiv \int_A E(y) y^2 dA \Rightarrow \frac{M}{\overline{EI}} = \kappa$ OR $M = k_B \kappa$

Beam equation:

$$\kappa \approx \frac{d^2u}{dx^2}$$

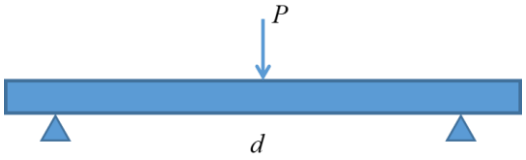

Mid-point : $x = \frac{d}{2}$

Simply supported beam → Mid-point displacement:

Beam stiffness:

$$k_B = \overline{EI} = \frac{M_{\max} d^2}{12\delta_{mid}} = \frac{Pd^3}{48\delta_{mid}}$$

$$\delta_{mid} = \frac{Pd^3}{48\overline{EI}} = \frac{M_{\max} d^2}{12\overline{EI}}$$

Max curvature:

$$\kappa_{\max} \equiv \frac{M_{\max}}{\overline{EI}} = \frac{M_{\max}}{\frac{M_{\max} d^2}{12\delta_{\max}}} \Rightarrow \kappa_{\max} = \frac{12\delta_{\max}}{d^2}$$

Strain energy density:

$$U \equiv \frac{1}{2V}\int_V \sigma\varepsilon dV$$

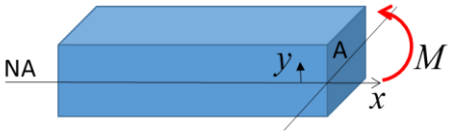

In a sliver of cross section:

$$V = A\Delta x$$

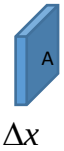

$$U \approx \frac{1}{2A\Delta x}\int_V \sigma\varepsilon dA\Delta x = \frac{1}{2A}\int_V \sigma\varepsilon dA = \frac{1}{2A}\int_V E\varepsilon^2 dA$$

Considering the cross section under the load:

$$x = \frac{d}{2}$$

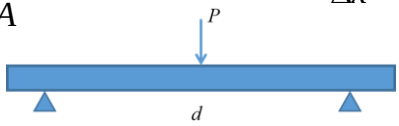

$$\Rightarrow U_{\max} = \frac{\kappa_{\max}^2}{2A}\overline{EI} = \frac{\kappa_{\max}^2}{2A} \times \frac{M_{\max}}{\kappa_{\max}} = \frac{\kappa_{\max} M_{\max}}{2A}$$

$$\Rightarrow U_{\max} = \frac{\kappa_{\max} M_{\max}}{2A} = \frac{\kappa_{\max} M_{\max}}{2tW}$$

6. Bending of the sample after detachment

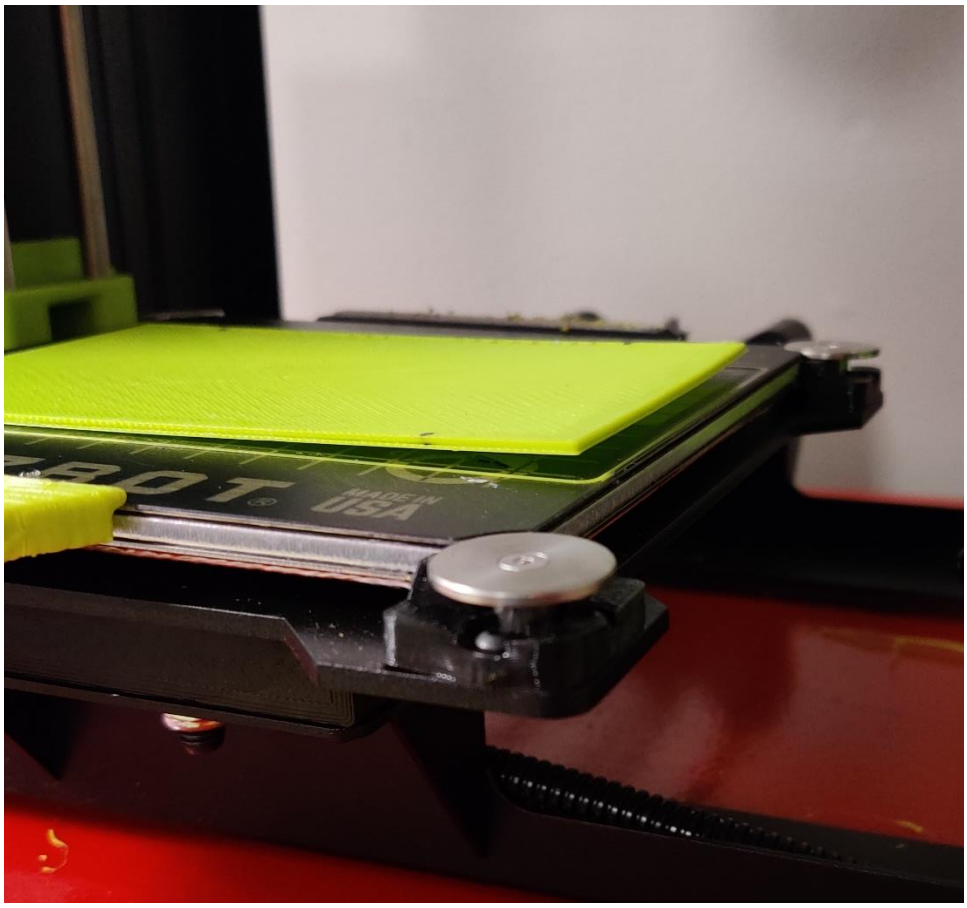

7. Powerlite DLS Plus Nd:YAG